Science Advances
AAAS

Supplementary Materials for

Fossil records of early solar irradiation and cosmolocation of the CAI factory: A reappraisal

David V. Bekaert*, Maureen Auro, Quinn R. Shollenberger, Ming-Chang Liu, Horst Marschall, Kevin W. Burton, Benjamin Jacobsen, Gregory A. Brennecka, Glenn J. MacPherson, Richard von Mutius, Adam Sarafian, Sune G. Nielsen

*Corresponding author. Email: dbekaert@whoi.edu

Published 29 September 2021, *Sci. Adv.* **7**, eabg8329 (2021)
DOI: 10.1126/sciadv.abg8329

This PDF file includes:

S1) Sample description

Sample name	Smithsonian nomenclature	Host meteorite	Texture	REE group
CAI75	USNM 3507-75	Allende (CV3)	coarse-grained	III
CAI3529	USNM 3529-42	Allende (CV3)	coarse-grained	III
CAI65	USNM 3507-65	Allende (CV3)	coarse-grained	I, V
CAI08	USNM 3507-8	Allende (CV3)	coarse-grained	I, V
CAI30	USNM 3507-30	Allende (CV3)	coarse-grained	III
CAI01	-	Allende (CV3)	fine-grained	II
CAI02	-	Allende (CV3)	fine-grained	II
CAI03	-	Allende (CV3)	fine-grained	II

Table S1. Sample description. Backscattered electron images of CAI3529, CAI30, CAI08, CAI75, and CAI65 are reported in Figure S1.

Description of CAIs from the Smithsonian museum:

USNM 3507-8: Back-scatted electron image (Fig. S1-a1, a2) and Ca-Al-Mg element map (lower) of USNM 3507-8. This CAI is a typical Type B2 inclusion that once was molten, and consists mainly of melilite (Mel), fassaite pyroxene (Pyx), anorthite (An), and spinel (Sp). In the element maps, calcium is green, aluminum is blue, and magnesium is red. In this and subsequent element maps, melilite appears aqua to greenish-blue in color, spinel is pink, pyroxene is olive-green to brown, and anorthite is medium blue. The matrix (Mtx) is mostly olivine (red).

USNM 3507-30: Back-scatted electron image (Fig. S1-b1, b2) and Ca-Al-Mg element map (lower) of USNM 3507-30. This CAI is highly fragmented and is transitional in mineralogy and composition between a Compact Type A and a Type B. It probably solidified from a melt. The element map corresponds to the area outlined in red on the BSE image. The inclusion consists mainly of melilite, fassaite pyroxene, anorthite, and spinel. Abbreviations and element map colors as in USNM 3507-8, except the areas that are dark blue consist of secondary minerals such as nepheline and sodalite.

USNM 3507-65: Back-scatted electron image (Fig. S1-c1, c2) and Ca-Al-Mg element map (lower) of USNM 3507-65. This round CAI is a Type B, and solidified from a melt. The inclusion consists mainly of melilite, fassaite pyroxene, anorthite, and spinel. Abbreviations and element map colors are as used previously.

USNM 3507 75: Back-scatted electron image (Fig. S1-d1, d2) and Ca-Al-Mg element map (lower) of USNM 3507-75. This CAI is a heavily altered Type A; it is not clear if this CAI was ever molten or not. The inclusion consists mainly of melilite, hibonite (Hib), and spinel. Abbreviations and element map colors are as used previously except that hibonite is dark blue and secondary minerals are purplish-blue.

USNM 3529-42 Back-scattered electron image of USNM 3529-29 (Fig. S1-e). The inclusion is composite. On the right is a lithology that resembles a typical Fluffy Type A inclusion consisting of melilite with accessory spinel, and which is heavily altered to a fine-grained mixture of feldspathoids, anorthite, and grossular. The bulk of the CAI ("Spinel-rich intergrowth") is a very dense intergrowth of spinel, melilite, and hibonite; this lithology shows no secondary alteration. The two lithologies are intergrown at their boundary - this is not an accidental juxtaposition of two separate objects within the bulk meteorite.

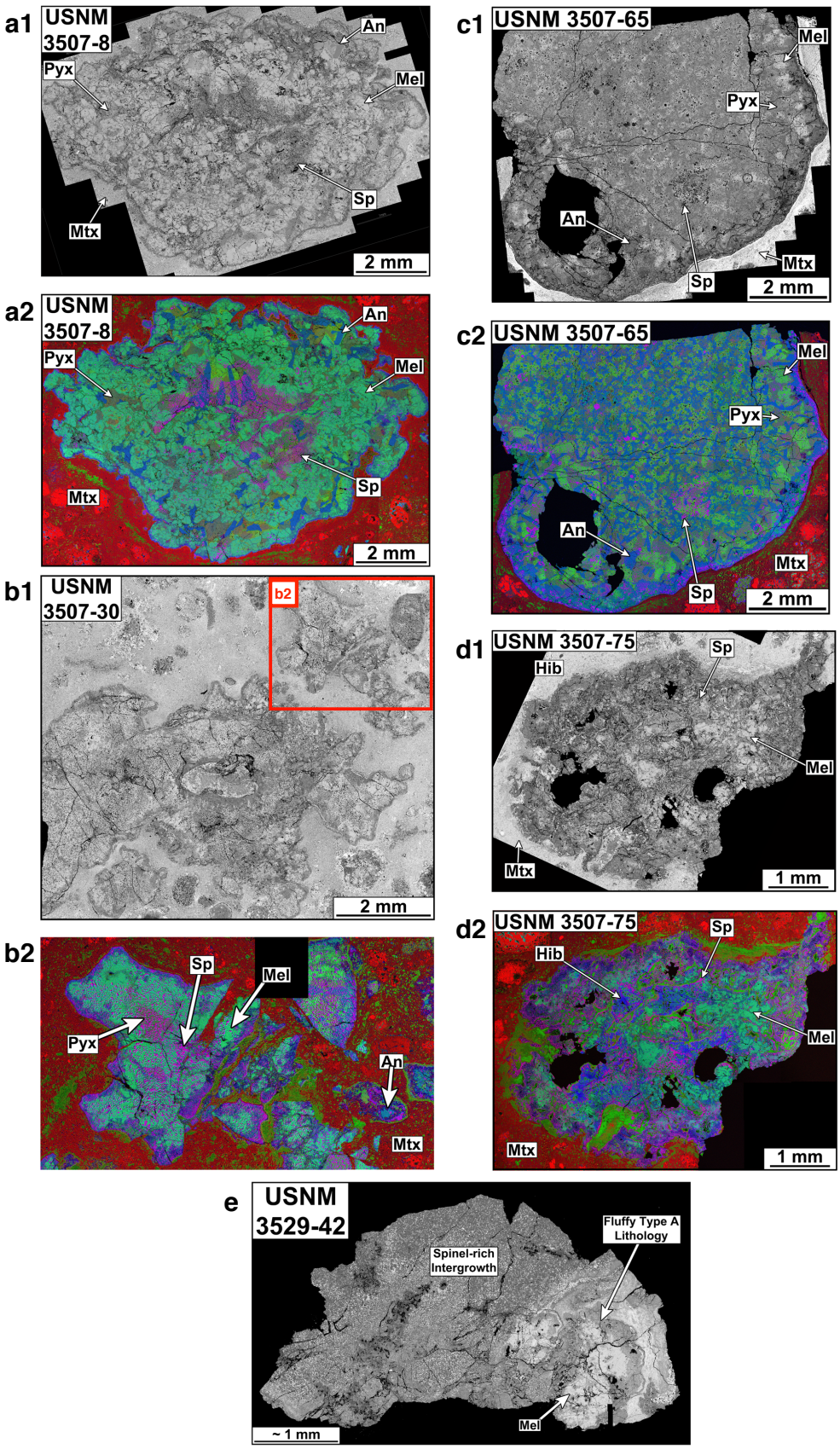

Figure S1: Backscattered electron images of CAI08 (a1, a2), CAI30 (b1, b2), CAI65 (c1, c2), CAI75 (d1, d2), and CAI3529 (e).

S2) Rare Earth Element patterns

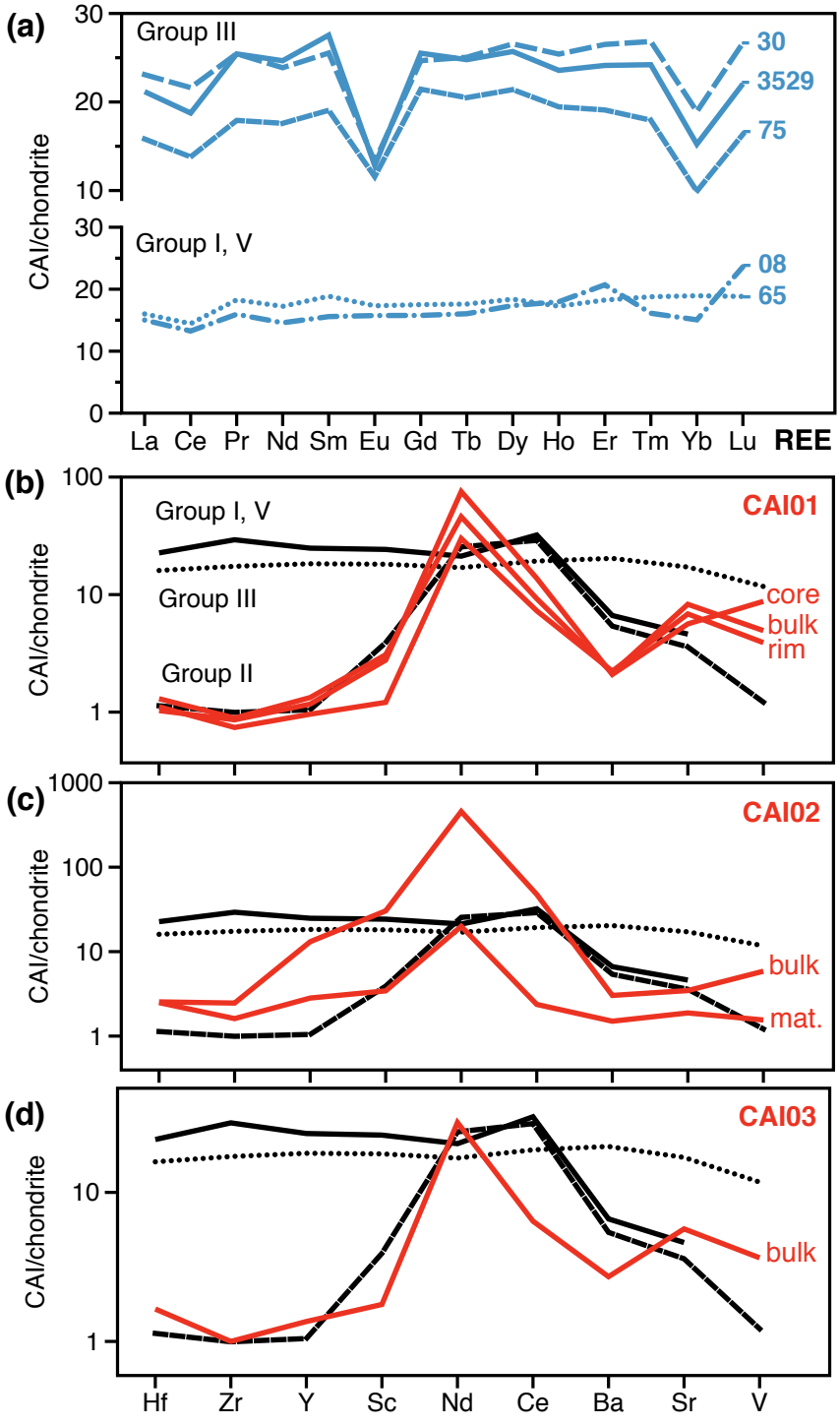

Figure S2: Rare Earth Element (a) and trace element (b-d) patterns of coarse- and fine-grained CAIs analyzed in this study. Coarse- and fine-grained CAIs are reported in blue and red, respectively. Line styles for panels (c) and (d) are the same as defined in panel (b), with reference trace element patterns for group I, V (solid line), III (dashed line) and II (dashed line) CAIs (data from Kornacki and Fegley (**59**)) being reported in black for comparison. "mat." refers to "matrix".

	Li	Na	Mg	Al	Ca
CAI30	n.d.	2758	58202	201561	179139
CAI 8	0.869	6653	68888	106400	160322
CAI75	1.235	5064	28786	127997	148894
CAI3529-42	0.849	5912	29808	164486	177988
CAI65	0.861	2508	61506	120140	177620
	Sc	**Ti**	**V**	**Cr**	**Mn**
CAI30	164.6	13173	400.7	384.9	109.8
CAI 8	84.7	6347	444.1	979.6	416.2
CAI75	64.7	5256	206.2	207.0	74.5
CAI3529-42	58.6	4464	249.3	269.1	186.1
CAI65	82.5	6603	955.8	384.8	61.5
	Fe	**Co**	**Ni**	**Cu**	**Zn**
CAI30	13983	16.625	237.5	3.258	272.5
CAI 8	52268	75.342	1489.4	6.543	93.3
CAI75	11148	3.449	71.5	1.874	872.8
CAI3529-42	25797	30.472	666.3	3.320	275.4
CAI65	6322	8.674	149.5	1.011	58.8
	Rb	**Sr**	**Y**	**Mo**	**Cd**
CAI30	0.755	121.293	31.792	10.063	0.094
CAI 8	2.416	152.195	25.206	n.d.	0.378
CAI75	0.741	99.624	18.620	6.885	0.095
CAI3529-42	0.929	122.592	29.425	2.796	0.124
CAI65	0.387	157.316	20.729	4.597	0.099
	Cs	**Ba**	**La**	**Ce**	**Pr**
CAI30	0.020	22.142	5.358	13.43	2.36
CAI 8	0.098	52.079	3.486	8.23	1.48
CAI75	0.072	10.330	2.717	6.69	1.29
CAI3529-42	0.049	12.722	4.911	11.65	2.36
CAI65	0.011	60.912	3.714	8.96	1.70
	Nd	**Sm**	**Eu**	**Gd**	**Tb**
CAI30	10.91	3.70	0.72	4.88	0.89
CAI 8	6.67	2.26	0.86	3.12	0.57
CAI75	6.24	2.27	0.62	3.43	0.63
CAI3529-42	11.27	4.00	0.70	5.05	0.88
CAI65	7.87	2.74	0.95	3.47	0.63
	Dy	**Ho**	**Er**	**Tm**	**Yb**
CAI30	6.321	1.428	4.293	0.636	3.084
CAI 8	4.129	1.010	3.355	0.382	2.455
CAI75	4.587	1.010	2.953	0.425	2.030
CAI3529-42	6.116	1.325	3.910	0.574	2.483
CAI65	4.376	0.969	2.956	0.445	3.088
	Lu	**Tl**	**Pb**	**Th**	**U**
CAI30	0.632	n.d.	0.350	0.656	0.209
CAI 8	0.560	0.0069	0.376	0.479	0.050
CAI75	0.406	0.0028	0.243	0.281	0.043
CAI3529-42	0.522	0.0054	0.444	0.332	0.042
CAI65	0.446	0.0012	0.316	0.431	0.066

Table S2. iCap measurements of the elemental abundances (in µg/g) of major and rare earth elements in the CAIs analyzed in this study (at WHOI, MA, USA). n.d.: not determined.

	CAI 01	CAI 02	CAI-3
Li	0	1.45	2.12
Na	47264	23631	28277
Mg	101941	86466	84853
Al	125235	152520	68905
P	101	234	243
K	2474	1910	2003
Ca	111384	68009	81844
Sc	18.20	179.20	10.46
Ti	2435	2185	1947
V	268	318	198
Cr	1599	1093	1416
Mn	633	579	717
Fe	45396	64603	59676
Ni	564	1670	1709
Cu	4.00	7.99	8.39
Zn	195	759	125
Rb	14.41	6.42	7.61
Sr	64.61	27.04	44.47
Y	2.03	20.04	2.09
Zr	3.23	8.89	3.62
Mo	0.50	0.46	0.60
Cd	3.44	2.42	2.43
Ba	5.18	7.29	6.55
Ce	5.74	29.58	3.99
Nd	3.68	36.52	2.36
Hf	0.14	0.27	0.17
W	0.13	0.10	0.13
Re	0.03	0.03	0.04
Pb	0.162	0.58	0.16
Th	0.18	1.54	0.10
U	0.01	0.01	0.01

Table S3. iCap measurements of the elemental abundances (µg/g) of major and rare earth elements in the CAIs analyzed in this study (at Durham University, UK).

S3) V and Sr isotope data

Sample	Be	Ti	Cr	Fe	V	$\delta^{51}V$	2SD	*n*	$\delta^{88}Sr$	2SE
CAI 08	0.05	6347	980	52268	444	-1.31	0.14	*3*	-0.39	0.03
CAI30	0.05	13173	385	13983	401	-2.35	0.03	*2*	-1.82	0.04
CAI65	0.1	5982	355	5887	877	-0.96	0.03	*6*	0.05	0.03
CAI75	0.1	5256	207	11148	206	0.49	0.11	*3*	1.92	0.03
CAI3529	0.15	4464	269	25797	249	-0.49	0.07	*3*	0.63	0.03
CAI 01a		2067	1088	42842	212	-3.07	0.09	*3*	-1.50	0.03
CAI 01b		2435	1599	45396	268	-2.89	0.09	*4*	-0.42	0.03
CAI 02 Bulk		2185	1093	64603	318	-4.90	0.09	*4*	-0.80	0.03
CAI 03 Bulk		1947	1416	59676	198	-2.93	0.09	*3*	-2.93	0.03

Sample	$^{87}Sr/^{86}Sr$	2SE	$^{87}Rb/^{86}Sr$
CAI 08	0.701678	0.000007	0.051190
CAI30	0.700129	0.000012	0.020076
CAI65	0.699470	0.000002	0.007923
CAI75	0.701198	0.000004	0.023999
CAI3529	0.700548	0.000006	0.024441
CAI 01a	0.725189	0.000003	0.446260
CAI 01b	0.730779	0.000004	0.719540
CAI 02 Bulk	0.743693	0.000005	0.765601
CAI 03 Bulk	0.729189	0.000003	0.551726

Table S4. The $\delta^{51}V$ and $\delta^{88}Sr$ of each sample are reported together with concentrations of main target elements for cosmogenic production of V, in ppm. We also report the $^{87}Sr/^{86}Sr$ and $^{87}Rb/^{86}Sr$ of each analyzed CAI (see Fig. S3).

S4) Rb-Sr systematics

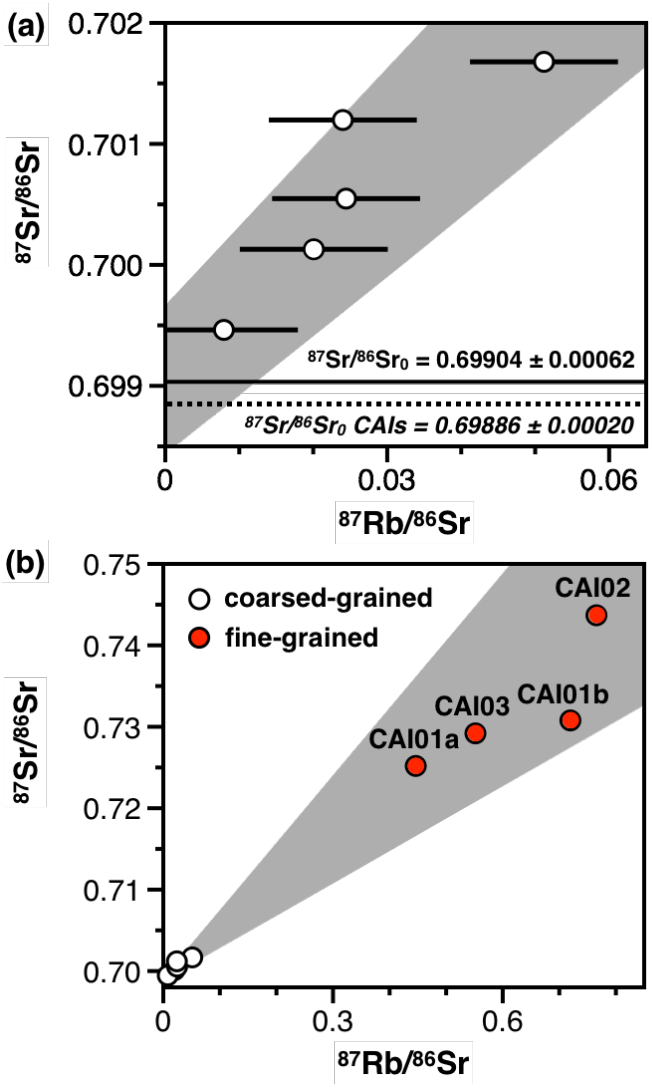

Figure S3: ^{87}Rb-^{86}Sr errorchron of CAIs investigated in this study. Coarse-grained CAIs define an errorchron corresponding to an age of 4.1 ± 0.7 Gyr (grey envelopes on panels a and b, MSWD: 2.6). The initial $^{87}Sr/^{86}Sr$ corresponding to this errorchon (0.69904 ± 0.00062 at 2σ, horizontal solid line, panel a) is similar to the canonical initial $^{87}Sr/^{86}Sr$ of CAIs (horizontal dashed line, panel a; **31**). Fine-grained CAIs, characterized by much higher $^{87}Rb/^{86}Sr$, appear to plot within the error envelope of the coarse-grained CAI errorchron. The observed scatter in the full data set may be indicative of open system processes (e.g. decoupling of Rb from Sr during alteration, later addition of Rb during impact events) and/or physical admixture of matrix during sampling of the CAIs (**31**). Sr concentrations were determined by isotope dilution from the double spike Sr isotope measurements, whereas the Rb concentrations were determined by ICP-MS at WHOI. Corresponding data are reported in Table S2.

S5) ^{26}Al-^{26}Mg systematics

After splits of 5 to 15 mg of CAI fragments had been handpicked for V and Sr isotope analyses, a second set of CAI fragments was selected for SIMS analyses (Be–B and Al–Mg). Because the most pristine chips were used for V and Sr isotope analyses, CAI fragments for SIMS analyses were more likely to represent rim fragments eventually associated with matrix. This potentially explains – at least to some extent – the dispersion of SIMS data. These chips were first mounted in epoxy for coarse polishing, and then mounted in indium for careful, fine polishing using diamond paste.

^{26}Al-^{26}Mg measurements were carried out on four coarse-grained CAIs following the analytical procedure described in Liu et al. (**108**). Although some debate remains regarding the extent of ^{26}Al heterogeneity in the early Solar System (e.g., **80,109**), a canonical ^{26}Al/^{27}Al of ~5×10^{-5} is generally considered as the Solar System initial ratio (noted ^{26}Al/^{27}Al$_0$), which represents "time zero" for high-resolution relative chronometry of the Solar System's oldest solids (**76,110,111**). Here, all ^{26}Al/^{27}Al$_0$ are associated with large uncertainties compared to literature data due to limited spreads in measured ^{27}Al/^{24}Mg values (Fig. S4). Despite large dispersion of the data, two coarse-grained CAIs (CAI08 and CAI65) show (^{26}Al/^{27}Al)$_0$ in first-order agreement with the canonical value. The Al-Mg systematics of CAIs 3529 and 75 do not provide any meaningful chronological information.

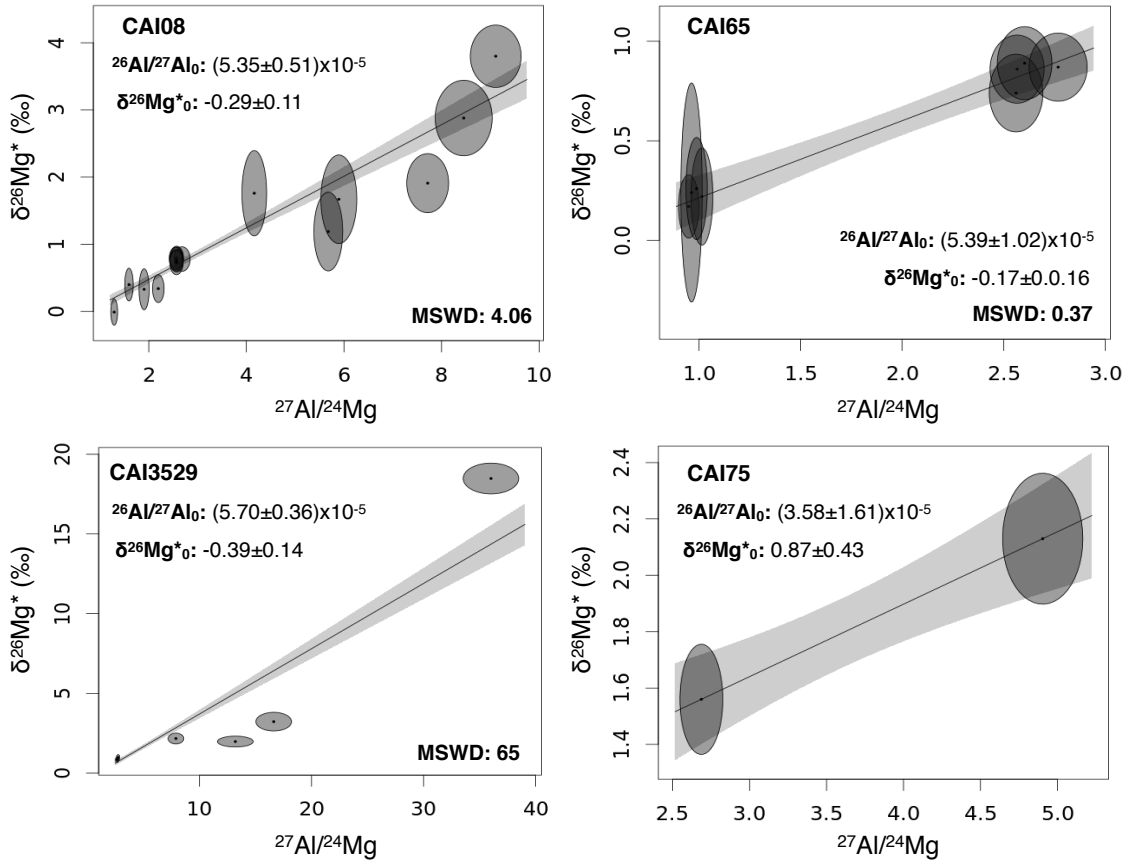

Figure S4. Al–Mg isochrons determined for coarse-grained samples CAI08 (a), CAI65 (b), CAI3529 (c), and CAI75 (d). On each panel, the dashed line and associated 2σ envelope represent the error-weighted least square fit through the data (**90**). Corresponding slope and y-intercept are reported together with their associated 2σ uncertainties on the top left corner of each panel. MSWD values are reported on bottom right corners. Uncertainties are shown at 2σ.

Sample	$^{27}Al/^{24}Mg$	2σ	$\delta^{26}Mg^*$	2σ
CAI 08				
1 (Spinel)	2.573	0.113	0.80	0.14
2 (Spinel)	2.682	0.135	0.78	0.15
3 (Spinel)	2.571	0.113	0.77	0.15
4 (Pyroxene)	1.594	0.071	0.40	0.20
5 (Pyroxene)	1.291	0.057	-0.01	0.16
6 (Melilite)	7.716	0.351	1.91	0.36
7 (Melilite)	9.110	0.426	3.80	0.38
8 (Melilite)	8.454	0.478	2.88	0.46
9 (Melilite)	5.679	0.242	1.19	0.48
10 (Spinel)	2.556	0.112	0.79	0.14
11 (Spinel)	2.568	0.112	0.76	0.13
12 (Melilite)	4.162	0.207	1.76	0.52
13 (Spinel)	2.568	0.112	0.73	0.15
14 (Pyroxene)	1.904	0.085	0.33	0.25
15 (Melilite)	5.895	0.301	1.67	0.54
16 (Pyroxene)	2.195	0.097	0.34	0.17
CAI 3529				
1 (Spinel)	2.627	0.116	0.83	0.14
2 (Spinel)	2.729	0.117	0.97	0.15
3 (Melilite)	36.021	2.029	18.48	0.79
4 (Melilite)	16.623	1.302	3.22	0.48
5 (Melilite)	13.195	1.306	1.97	0.28
6 (Melilite)	7.888	0.568	2.16	0.28
CAI 65	2.566	0.109	0.86	0.14
	2.561	0.108	0.74	0.16
	0.949	0.041	0.17	0.13
	1.014	0.044	0.22	0.20
	0.963	0.043	0.24	0.45
	0.988	0.043	0.26	0.21
	2.768	0.117	0.87	0.14
	2.603	0.110	0.89	0.15
CAI 75	2.687	0.114	1.56	0.16
	4.904	0.213	2.13	0.19

Table S5. Al-Mg data obtained for CAI 08, CAI 3529, CAI 65, and CAI 75 (Figure S4).

S6) Be-B measurements

a- Reference materials

Three different andesitic and komatiitic reference glasses were used in this study to determine the instrumental mass fractionation (IMF) for the boron isotope ratio and the $^{9}Be/^{11}B$ relative ion yield (RIY). These glasses were GOR128-G, GOR132-G, and StHs6/80-G with boron concentrations of approximately 12–23 µg/g and beryllium concentrations of 0.034–1.2 µg/g (**104,112,113**). Polishing was completed using a Buehler MiniMet 1000 polishing machine (1 µm diamond paste), which was set to produce a flat and even surface throughout the epoxy and glass samples. Alumina polish (0.3 µm) was used for the final polish. Prior to gold coating, the thin sections were cleaned using 96% ethanol followed by an ultrasound bath using distilled water from a Millipore ultrapure water system (18 MΩ). Samples were always cleaned and coated immediately before introducing them into the airlock of the mass spectrometer to reduce the possible deposition of contamination on the sample surfaces.

b- Contamination

Surface contamination has been identified as a potential obstacle in the determination of accurate B abundances and B isotope data in low-B concentration samples (**105,114,115**). It is critical to estimate the B amount and isotopic composition of the remaining surface contamination to quantify the possible bias introduced by the remaining contamination. Beryllium is not prone to surface contamination.

As in earlier studies, we use the silica glass Herasil-102 (Heraeus Quarzglas GmbH, Germany) to characterise B surface contamination. Previously, the B concentration of Herasil-102 was shown to be less than 1.1 ng/g (**105**). This value resulted from the combined contributions of surface contamination, machine background, memory effects, and B from the glass itself. Here, a fragment of Herasil-102 was mounted in epoxy and polished together with the B isotope reference materials and analyzed for apparent B isotopic composition using the same analytical setups. Boron isotope measurements on Herasil-102 corrected for machine background resulted in ion yields of 0.42 s^{-1} for ^{11}B. In the reference glasses (and samples), the same count rate amounts to a contamination contribution of 0.3 ng/g. Again, some of the signal detected on Herasil-102 may be B from the glass itself, such that the actual contamination level may still be lower than the value given here. The B isotopic composition of the surface contamination using Herasil-102 can only be determined with large uncertainty, due to the very low count rates, but is approximately 0.25 (i.e., typical terrestrial composition). A contamination composition of d $\delta^{11}B$ = -36±27‰ was reported by Marschall & Monteleone (**104**), which is used to estimate the maximum systematic error of B surface contamination on the B isotope analyses of the samples using a simple mixing approach (**104**).

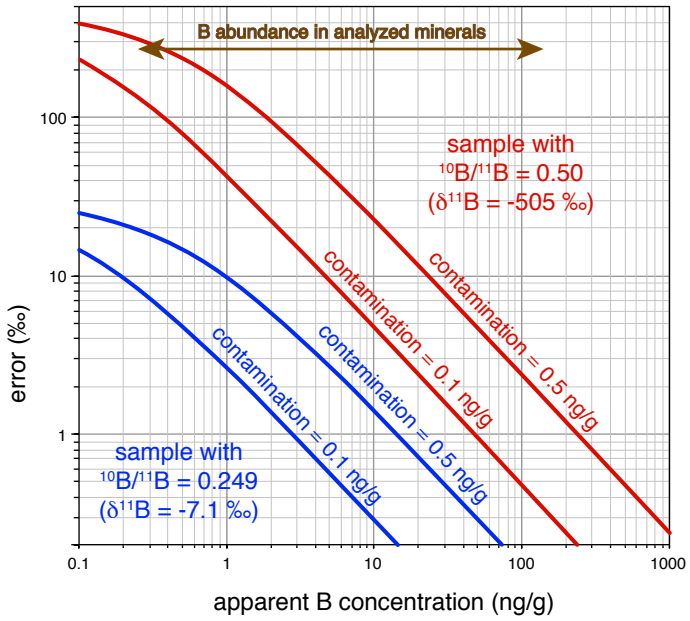

Figure S5. Potential systematic error introduced by boron contamination as a function of sample boron concentration for samples with a boron isotopic composition equal to the bulk-silicate Earth (blue lines; $^{10}B/^{11}B$ = 0.249) and a radiogenically enriched composition (red lines; $^{10}B/^{11}B$ = 0.50). Contamination equivalent to 0.5 ng/g or 0.1 ng/g were assumed with a B isotopic composition of $\delta^{11}B$ = -36‰ (**104**). The investigated CAI minerals contain 0.26–120 ng/g B.

The boron isotope bias generated by potential surface contamination with the near-terrestrial composition mentioned above is stronger on samples with a strong radiogenic component compared to samples that have a terrestrial composition themselves (Fig. S5). The lines displayed represent approximate upper limits for the systematic error, and further evidence shows that they may overestimate the contamination contribution in this study: (1) The analyses with the lowest B content show rather constant count rate signals over the duration of each individual analysis (Fig. S6) instead of the decreasing count rates that are typical for contamination-afflicted analyses (**105**). The count rates of the low-B analyses displayed in Fig. S6 are in the 0.2–0.8 s^{-1} range, similar to the Herasil-102 glass, but with radiogenic, distinctly non-terrestrial compositions. (2) The observation of strongly radiogenic compositions at low B concentrations shows that any influence of terrestrial B contamination in the analyses has to be small. (3) The measurement repeatability (precision) of all analyses presented in this study follow the values predicted by counting statistics (see below; Fig. S7), which would not be the case for sets of analyses afflicted with contamination (**105**).

Values in this study were not corrected for potential contamination. Any remaining contamination would pull the analyses with the lowest B content (i.e. the samples with the highest detectable radiogenic component) towards the terrestrial composition in a $^{10}B/^{11}B$ versus $^{9}Be/^{11}B$ plot. It would thus decrease the spread of the data points but would have no significant effect on the estimated ^{10}Be activity for CAI that have an intersect (=initial $^{10}B/^{11}B$ ratio) close to the terrestrial value. Samples with higher B contents (lower $^{9}Be/^{11}B$) would be much less affected by contamination, such that the estimated intersect would also be affected to a very small degree only.

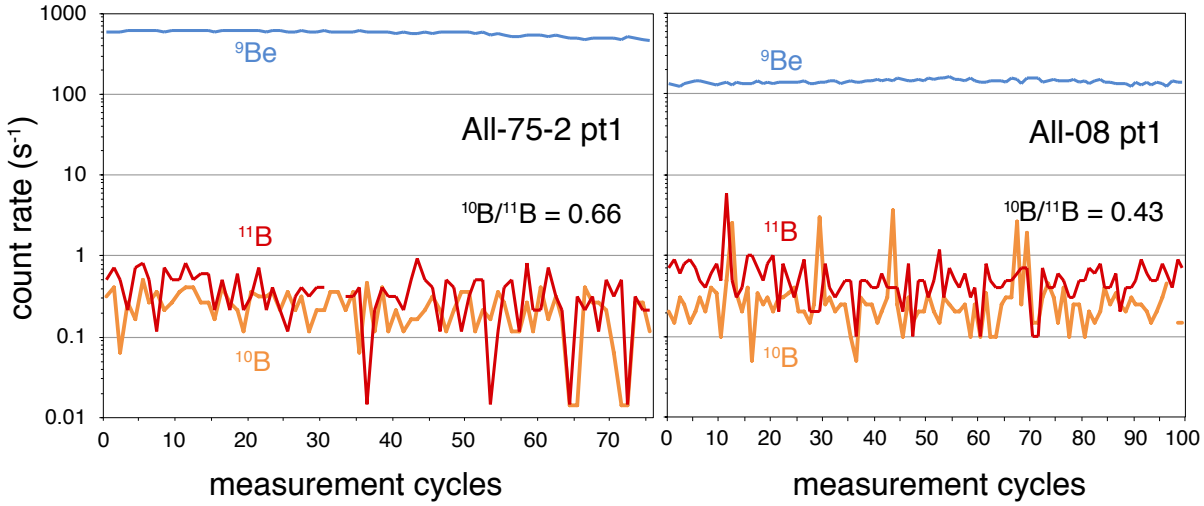

Figure S6. Recorded background-corrected count rates of ^{9}Be (blue line), ^{10}B (orange-colored line) and ^{11}B (red line) of two analyses with 77 and 100 measurement cycles, respectively. These are the two analyses with the lowest B count rates. Note that count rates of the two boron isotopes do not show any systematic decrease, demonstrating that surface contamination was insignificant in our study, even for the analyses with lowest boron-concentration samples.

c- Precision

The internal precision of a single spot isotope ratio analysis (measurement repeatability) is defined here as the standard error of the mean (SE = SD/ SQRT(n-1)) of the n-1 intensity-corrected ^{10}B/^{11}B ratios and are given here as two times the relative standard error (Fig. S7). The sensitivity of the instrument was 133 and 46 counts/s/nA/(µg/g) for ^{9}Be and ^{11}B, respectively, as determined using the reference glasses. The resulting predicted precisions for 50, 100, and 250 cycles are displayed in Fig. S7. This figure also shows the precision of analyses of the reference materials and the analyzed samples. Observed and predicted precisions agree well.

d- Analytical drift

Marschall & Monteleone (**104**) reported long-term drift of the instrumental mass fractionation (IMF) during B isotope ratio measurements over the course of a day of typically ±0.1‰/h. In both analytical sessions, over 48 and 22 h, respectively, from which data are reported in this study, the long-term drift was indistinguishable from ±0.0 ‰/h; hence, no long-term drift correction was applied to the data. Marschall & Monteleone (**104**) demonstrated that no systematic drift occurs for a boron isotope ratio measurement during a 40-cycle analysis under the current setup and analytical protocol. Here we report data collected using a higher number of cycles (40–100). In order to detect possible drift within the analysis of one spot, we completed one analysis with 248 cycles and analyzed it for possible down-hole drift (Fig. S8). The downhole drift in this analysis was insignificant with neither increasing nor decreasing count rates. Small-scale variations in count rates are interpreted as true sample heterogeneity (see below).

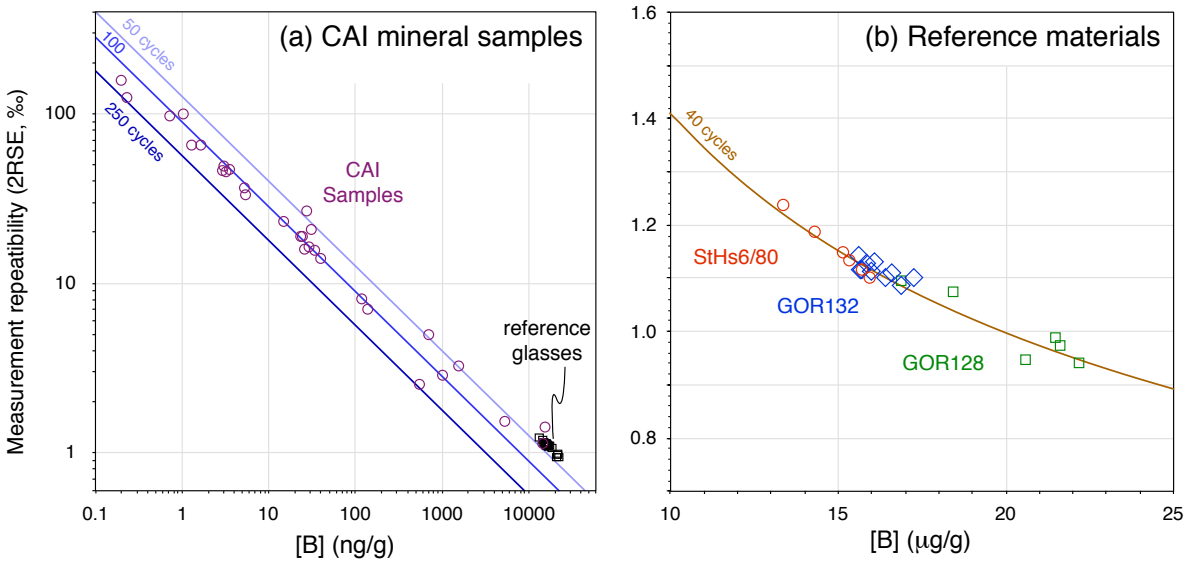

Figure S7. Measurement repeatability (”internal precision”) of individual B isotope determinations expressed as two times the relative standard error, as a function of boron concentration estimated from ^{11}B count rates. 100 measurement cycles were integrated for most analyses, but between 40 and 248 cycles were used in some cases. (b) Magnified portion of (a) displaying just the reference materials for which 40 measurement cycles were integrated. Note logarithmic scales and [B] in (ng/g) in (a) versus linear scales and [B] in (µg/g) in (b). Observed precisions agree with precisions predicted from Poisson statistics.

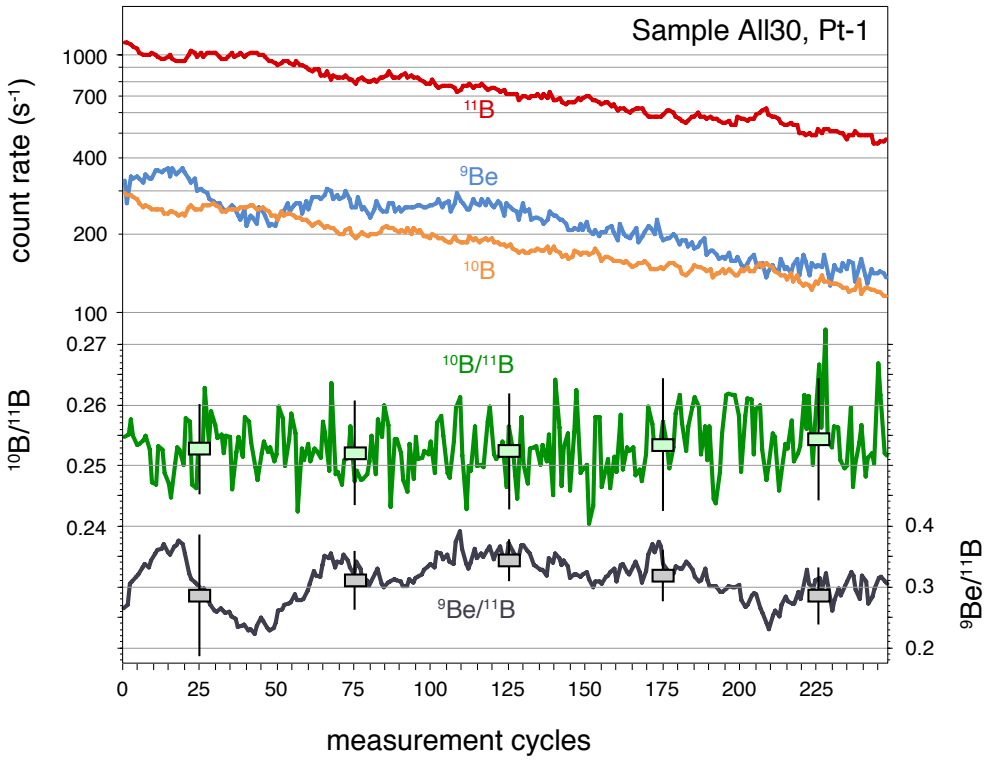

Figure S8. One spot analysis with 248 measurement cycles showing the background-corrected count rates of ^{9}Be (blue line), ^{10}B (orange line) and ^{11}B (red line), ^{10}B/^{11}B (green line), and ^{9}Be/^{11}B (black line) ratios resulting from these count rates. Also displayed are the isotope ratio means and uncertainty (2SD) of every 50 cycles of the analysis (squares and error bars). Note that ^{10}B/^{11}B ratios are constant, despite the downhole decrease of count rates. Beryllium count rates and ^{9}Be/^{11}B ratios vary significantly over the 248 cycles.

e- Matrix effects and accuracy

The matrix effect describes the dependency of the instrumental mass fractionation on the chemical composition or crystallographic structure of the analyzed materials. Matrix effects for B isotopes have been reported to be very small for a large range of minerals and glasses (**115-119**). For the settings used in this study, Marschall & Monteleone (**104**) showed that the matrix effect for a set of natural silicate glasses ranging from komatiitic to rhyolitic in composition was well within the repeatability of the B isotope analyses on these materials, i.e., that matrix effects were much smaller than 0.5‰. Marschall & Monteleone (**104**) report that reproducibility and accuracy for the reference glasses were within ±0.4 to ±1.6 ‰ (2RSD) including all internal and external uncertainties with a mean of ±1.0 ‰. We assume that the analyzed silicate and oxide minerals adhere to the same limits, but this was not tested due to a lack of suitable reference materials.

f- Sample heterogeneity

Here, we observed significant heterogeneity of the samples on the scale of the depth increase of an individual SIMS spot. This heterogeneity is most apparent in long-wavelength fluctuations (over tens of cycles) of the ^{9}Be (and boron) count rate and ^{9}Be/^{11}B ratio (see Fig. S8). These fluctuations are interpreted as a small-scale chemical zonation in Be (and/or B) in the respective mineral grains and are deemed acceptable. Yet in some cases, the count rates are characterized by massive jumps by more than an order of magnitude within one or two analytical cycles (e.g., Fig. S9). These discontinuities are interpreted as the boundary between two different minerals, such that the mineral grain exposed at the surface terminates at depth and the ion beam samples the grain located beneath. In such cases, only the first part of the profile was evaluated, whereas the discontinuity and subsequent cycles were discarded.

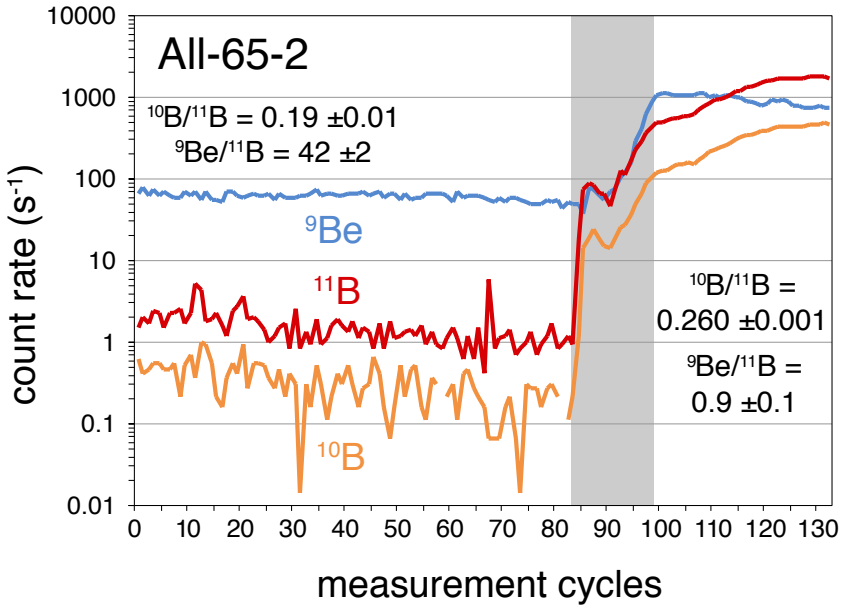

Figure S9. Recorded background-corrected count rates of ^{9}Be (blue line), ^{10}B (orange line), and ^{11}B (red line) of an analysis with 132 measurement cycles. There clearly is a strong discontinuity in the composition of the analyzed material that was pierced between cycles 84 and 100. In this example, determining where exactly we sputter the mineral of interest (melilite) and where we start to sputter into a grain-boundary region that could possibly be influenced by B derived from the chondrite matrix, is challenging. Due to large uncertainties associated with interpreting this profile, the point has been excluded for interpretations (Table S4). We also note that the $^{10}B/^{11}B$ computed from the first part of this analysis (cycles 1–84) is anomalously low (below the non-radiogenic initial value; Table S4), the cause of which remains unknown.

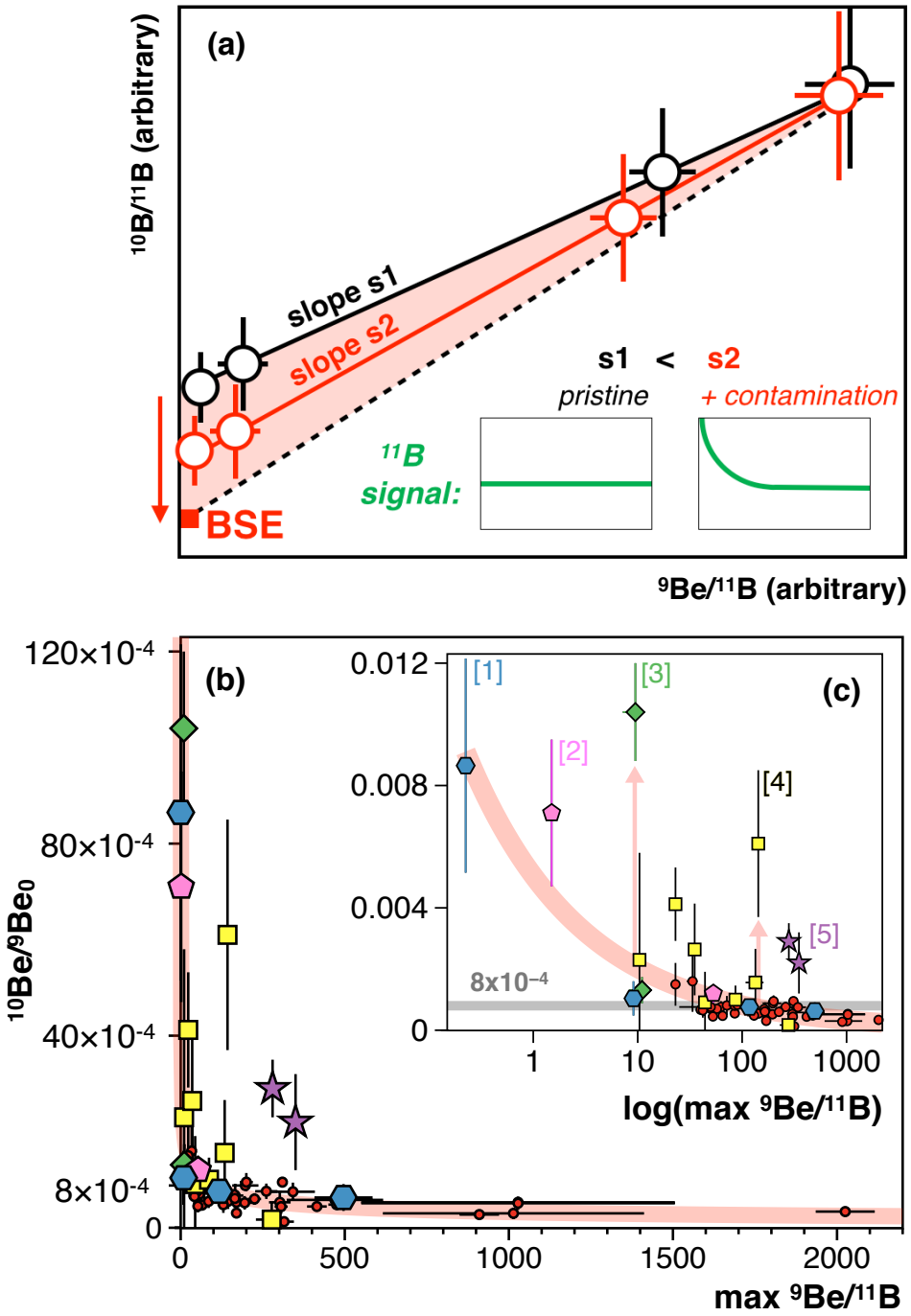

Figure S10: (a) Schematic representation of the potential for terrestrial contamination to produce overestimated ^{10}Be/^{9}Be values (computed from the slope of the isochrons). The red area represents the range of possible values corresponding to the addition of terrestrial and/or chondritic contamination from a pristine composition (black points). Red points materialize an example of contaminated sample, producing a virtually larger slope (s2) than the pristine isochron (s1). Arbitrary uncertainties are given for illustrative purpose. **(b)** Initial slopes of ^{10}Be-^{10}B isochrons in CAIs (^{10}Be/^{9}Be$_0$) as a function of the maximum associated ^{9}Be/^{11}B. Red dots are data for CV3 CAIs from literature. Blue hexagons [1] and pink pentagons [2] are data for CV3 CAIs from this study and Sossi et al. (**21**), respectively. Green diamonds [3] and yellow squares [4] are CB/CH CAIs from Gounelle et al. (**64**) and Fukuda et al. (**65**), respectively. Purple stars [5] are CO CAIs from Fukuda et al. (**66**). The red curve corresponds to a power law fit through the data. Panel (c) shows a zoomed in view of panel (b) using a log scale for the x-axis. Horizontal grey line shows ^{10}Be/^{9}Be$_0$ = 8x10^{-4}.

Sample	Mineral	$^{9}Be/^{11}B$	2σ	$^{10}B/^{11}B$	2σ	ρ_0
CAI 75		496	88	0.64	0.28	0.74
		2.218	0.056	0.2569	0.0042	0.69
		35.8	2.5	0.282	0.014	0.74
		125.04	7.87	0.329	0.024	0.70
		2.51	0.13	0.2537	0.0041	0.67
		19.56	0.78	0.261	0.011	0.59
CAI 65	anorthite	4.31	0.29	0.252	0.011	0.64
	melilite	4.17	0.13	0.245	0.011	0.46
	spinel	0.948	0.032	0.2502	0.0037	0.57
	melilite	9.11	0.12	0.2589	0.0051	0.56
	melilite	5.86	0.21	0.2530	0.0058	0.64
	melilite	5.20	0.13	0.2535	0.0056	0.60
	melilite	1.206	0.020	0.2485	0.0023	0.48
	melilite	2.433	0.079	0.2493	0.0090	0.68
	melilite	5.561	0.092	0.2520	0.0041	0.42
	melilite	*14.8*	*1.4*	*0.186*	*0.0020*	*0.57*
CAI 08	pyroxene	117	18	0.42	0.26	0.50
	pyroxene	20.5	1.1	0.285	0.021	0.57
	pyroxene	55.1	5.6	0.262	0.034	0.61
	pyroxene	0.656	0.020	0.2497	0.0040	0.69
	melilite	10.87	0.22	0.2675	0.0058	0.62
	melilite	41.9	1.6	0.276	0.015	0.41
	anorthite	4.96	0.23	0.284	0.024	0.52
CAI 3529		0.2252	0.0060	0.2514	0.0008	0.48
		0.2080	0.0071	0.2531	0.0013	0.52
		0.0518	0.0012	0.2527	0.0007	0.44
		0.0448	0.0029	0.2514	0.0015	0.43
		0.0055	0.0002	0.2493	0.0004	0.52
		0.0231	0.0007	0.2513	0.0005	0.30

Table S6. Be-B data obtained for CAI 75, CAI 65, CAI 08, and CAI 3529 (Figure 2). ρ_0 coefficients correspond to the so-called "coefficients of spurious correlation" used to compute the correlated uncertainties shown in Figure 2. The last data point for CAI 65 (in italic) represents the analysis reported in Fig. S9, corresponding to an anomalously low $^{10}B/^{11}B$ (below the non-radiogenic initial value) that cannot be explained straightforwardly. This data point has therefore been excluded for interpretations.

S7) Leaching experiments

At the University of Münster, approximately 6 g of the Murchison meteorite powder, provided by the Field Museum in Chicago, was processed through a six-step sequential acid leaching procedure described below (**120**).

Step 1) 25mL acetic acid + 25mL H_2O, 1 day, 20°C
Step 2) 12.5mL HNO_3 + 25mL H_2O, 5 days, 20°C
Step 3) 15mL HCl + 17.5mL H_2O, 1 day, 75°C
Step 4) 15mL HF + 7.5mL HCl + 7.5mL H_2O, 1 day, 75°C
Step 5) 7.5mL HF + 7.5mL HCl, 3 days, 150°C
Step 6) 7mL HNO_3 + 14mL HF + 400µL $HClO_4$, 5 days, 200°C
Dry down at 180°C to remove $HClO_4$
Treat the sample with ~5mL concentrated HNO_3
Dry down at 200°C to remove $HClO_4$ (repeat 4 times)
14mL HNO_3 + 7mL HCl, 2 days, 150°C

Following the leaching procedure, ~5% of each leachate solution was set aside for V isotope work. These solutions were evaporated to dryness and prepared for chemical separation of V (see analytical procedure for V isotope measurements). Sequential acid leaching experiments carried out on the Murchison CM2 chondrite show no V isotope variation (Fig. S11). Previous work has reported large Dy and Er nucleosynthetic anomalies on the same Murchison leachates that were most likely generated from the dissolution of presolar silicon carbide (SiC) grains (**32**). However, even for the more chemically aggressive leaching steps (i.e., L6) that concentrate certain presolar phases like SiC, the V isotope composition is unresolved from the bulk chondrite composition. Previous acid leaching studies have reported isotopic anomalies for many elements, including Ca, Cr, Sr, Zr, Mo, Ru, Ba, Nd, Sm, Hf, W, Os, Dy, Er, and Yb (**120-133**). Here, the absence of nucleosynthetic V variations in Murchison leachates and chondrites justifies the use of a single chondritic value, corresponding to the mean $\delta^{51}V$ composition of chondrites corrected for spallation-produced ^{50}V ($\delta^{51}V_{chondrites}$ = −1.089 ± 0.029 ‰; **34**), as the starting composition for the protosolar nebula.

Leachate	^{51}V [µg/g]	^{51}V (%)	$\delta^{51}V$	2SD	n
L1	8	16%	n.d.	-	0
L2	22	43%	-0.99	0.13	9
L3	5	10%	-1.14	0.08	5
L4	5	10%	-0.91	0.09	5
L5	4	8%	-0.99	0.17	4
L6	7	13%	-1.12	0.17	4

Table S7. Vanadium elemental and isotopic data obtained from experiments of acid leaching of the Murchison meteorite (Figure S11). Concentrations in the leachates were calculated by dividing the quantity of V in the leachate by the total mass of the Murchison sample.

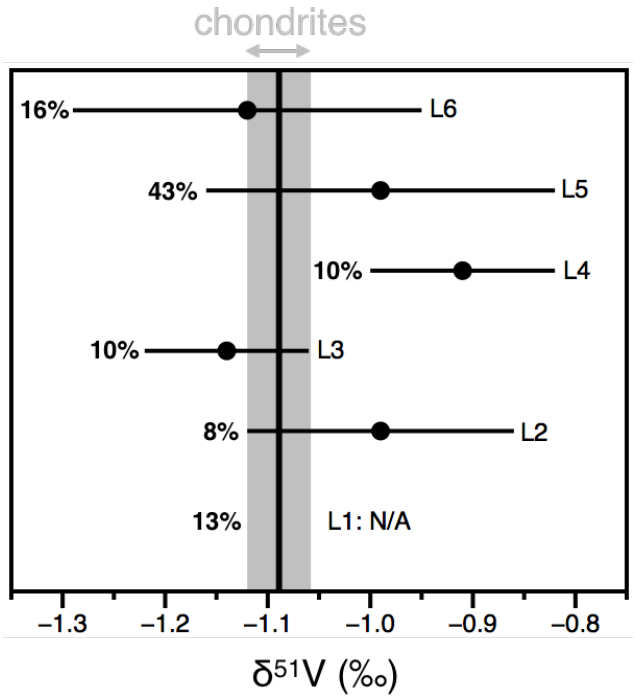

Figure S11: $\delta^{51}V$ isotope composition of Murchison (CM2) chondrite leachates (from L1 to L6, with L6 corresponding to the most chemically aggressive leachate) compared to the mean and 95 % c.i. composition of chondrites (**34**). Percentages on the left side of each data point refer to the fraction of total V that is released for each step of the leaching procedure. The slightly heavy V isotope composition of L4 could potentially be attributed to a small nucleosynthetic anomaly, the presence of a mineral phase that is enriched in heavy isotopes due to for instance evaporation, and/or isotopic fractionation during the leaching procedure. Here, no trend of isotopic enrichments is observed throughout the leaching process, which is indicative of negligible nucleosynthetic anomalies (≤0.2 ‰) being present for V in chondrites. Note that L1 was not analyzed for V isotopes due to extremely high cation concentrations.

S8) Kinetic fractionation modeling

In this paper, we use the mathematical formulation of kinetic isotopic fractionation during evaporation and condensation, as formulated by Richter (**54**), to model and interpret the observed co-variation of V and Sr isotopes in CAIs. In the case of free evaporation, the condensed phase and the gas reservoir represent the source and the sink, respectively, whereas for condensation, the gas is the source and the condensed phase the sink. The $\delta^{51}V$ and $\delta^{88}Sr$ dependencies on f are represented in Fig. S12, where the isotopic composition of each increment added to the sink (instantaneous flux) is 1000 x (α-1) ‰ lighter than the source.

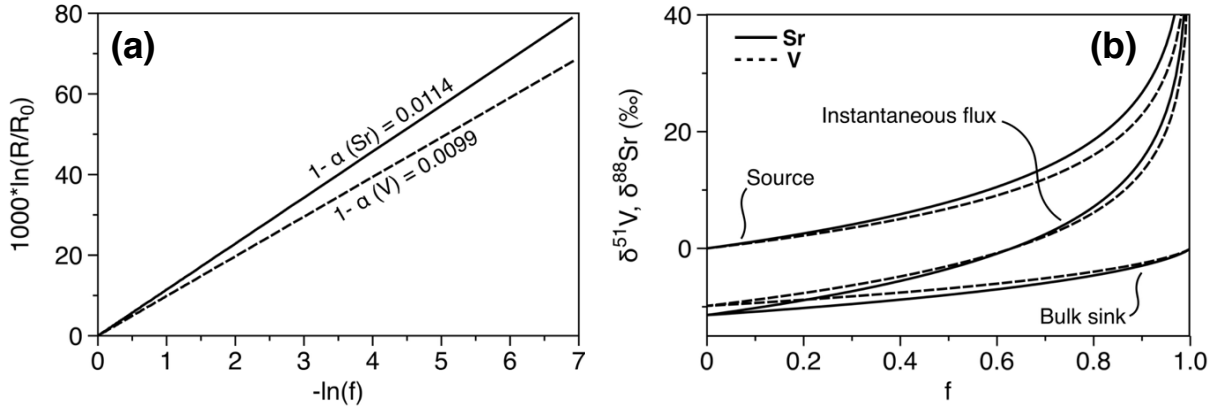

Figure. S12: Theory of kinetic isotopic fractionation (Richter 2004) applied to V and Sr. **(a)** Rayleigh fractionation produces here a straight line with intercept (0,0) and slope 1000x(1- α). The α values are 0.9886 and 0.9901 for Sr and V, respectively, based on the relative mass differences of the isotope pairs ^{51}V and ^{50}V, and ^{88}Sr and ^{86}Sr, respectively **(b)** The three curves plotted in this figure are, respectively, the isotopic composition of a Rayleigh fractionating source (condensed phase in the case of evaporation, gas in the case of condensation), the bulk sink (condensed phase in the case of condensation, gas in the case of evaporation), and the instantaneous flux from source to sink, plotted as a function of the fraction f of the original Sr or V remaining in the sink.

In a kinetically controlled process, an evaporation residue will be variably enriched in the heavy isotopes, depending on the degree of evaporative loss and on the gas/condensed phase isotopic fractionation factor. In contrast, a condensate formed under kinetic control tends to be enriched in light isotopes. Here we model these processes by following the mathematical formulation of kinetic isotopic fractionation during evaporation and condensation presented by Richter (**54**). Evaporation and condensation are considered in limiting case regimes where the gas is either under-saturated ($P_i < P_{i,sat}$) or super-saturated ($P_i > P_{i,sat}$), respectively, where P_i and $P_{i,sat}$ represent the partial pressure of species i and saturation vapor pressure, respectively. The kinetic isotope fractionation factor, α_{12}^{Kin}, between two isotopically distinct gas species of mass m_1 and m_2 is given by Eq. S1:

$$\alpha_{12}^{Kin} = (\gamma_1/\gamma_2)\sqrt{\frac{m_2}{m_1}} \qquad \text{(Eq. S1)}$$

where γ_i is the "evaporation" or "sticking" coefficient of species i. Here we assume that all processes considered in this paper involve sufficiently high temperatures (T > 1000 K) that equilibrium isotope fractionations can be neglected (**54**). Whereas the ratio of sticking coefficients could also have a significant effect on elemental fractionations, sticking coefficients for isotopes of the same element are assumed to be the same, such that α_{12}^{Kin}

can be simply expressed as $\sqrt{\frac{m_2}{m_1}}$. This isotope fractionation factor is the key quantity relating the isotopic fractionations of an evaporation residue to the amount of parent element evaporated. Using the usual formulation of the Rayleigh fractionation equation in the case of evaporation (i.e., where the partial pressure of the corresponding gaseous species i is small relative to its saturation vapor pressure), it follows that (Eq. S2):

$$\frac{R_{12}}{R_0} = f^{\alpha_{12}-1} \quad \text{(Eq. S2)}$$

where R_0 is the isotopic ratio N_1/N_2 in the condensed phase prior to evaporation and R_{12} is the isotopic ratio in the evaporation residue when a fraction f of a given isotope remains (**54**). In the case where the gas pressure is significantly greater than the saturation vapour pressure (i.e., in the case of condensation from a supersaturated gas phase), the condensate has a bulk isotopic composition given by Eq. S3:

$$\frac{R_{12}}{R_0} = \frac{(1-f^{\alpha_{12}})}{(1-f)} \quad \text{(Eq. S3)}$$

where R_{12} is the isotopic ratio in the condensate, R_0 is the initial ratio in the gas, and f is the fractional amount of a given isotope remaining in the gas. Rayleigh fractionation equations (Eq. S2 and S3) are used here to predict the isotopic composition of CAIs produced by partial condensation and evaporation, starting from a nebular gaseous reservoir of chondritic isotopic composition (Fig. 3 and Fig. S13a). We note that, in this approach, the sticking coefficients (γ_i; Eq. S1) of V and Sr are not known. Different γ_i values for V and Sr could significantly modify the slope of the modeled condensation/evaporation curves.

We note that taking the f (V) – f (Sr) relationship given in Table 1 for condensation of V and Sr, and combining it with the Rayleigh distillation during evaporation produces an expected evaporation trend that has a markedly different slope than the CAI correlation line (Fig. S14a). This indicates that different relationships between f (V) and f (Sr) are required during evaporation and condensation, which, in other words, implies that condensation and evaporation curves do not exactly mirror each other. Here, one possibility is that the slope of the CAI correlation line may only reflect evaporation - the opposite (only condensation) is impossible due to some CAIs being heavier than the chondritic composition. This scenario, however, would require all CAIs to have initially condensed to the almost exact same extent, as different extents of partial evaporation from condensates with different extents of partial condensation would not produce a linear correlation between the final residues (Fig. S14b). Alternatively, the condensation and evaporation trends could be close to one another, therefore resulting in the products of partial condensation and evaporation to roughly plot on a single line. We hypothesize that additional CAI data may ultimately reveal the existence of different slopes in the observed $\delta^{51}V$-$\delta^{88}Sr$ correlation, which are not resolvable at the present level of precision and/or with the present amount of data.

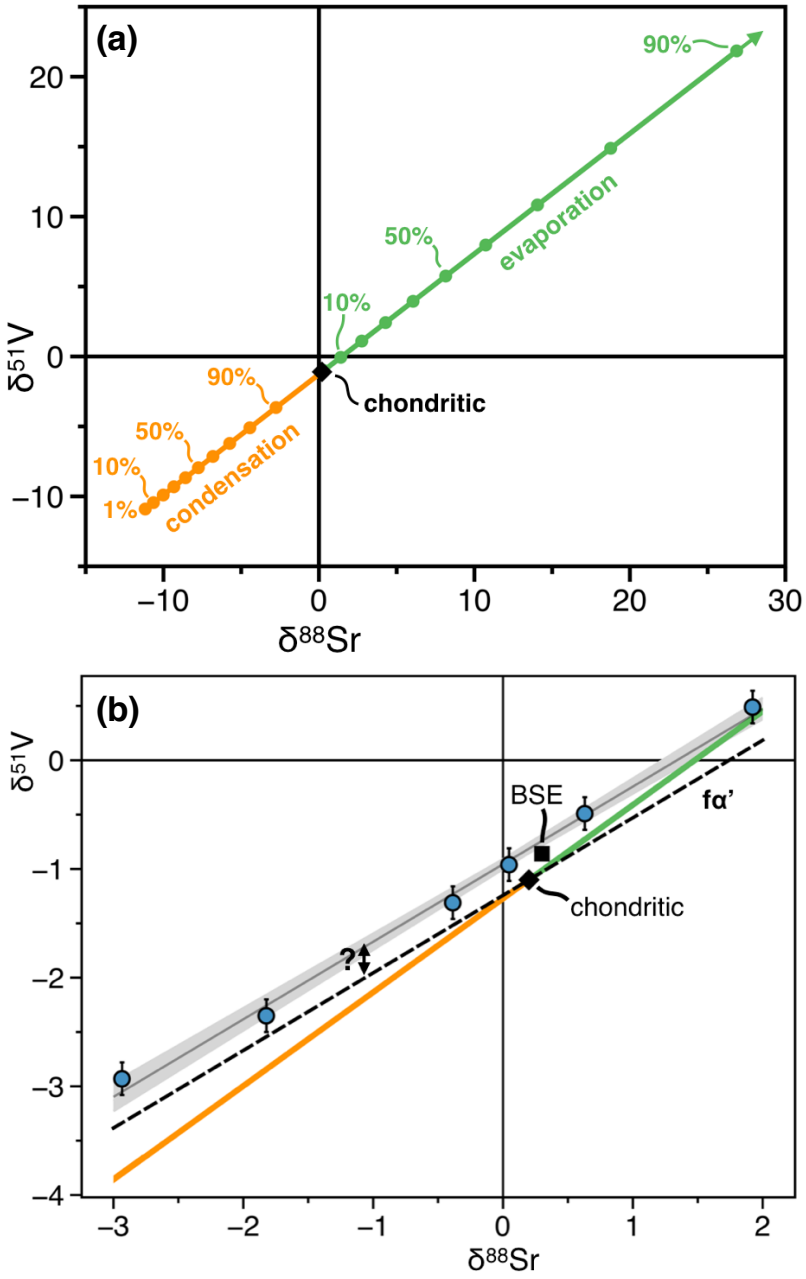

Figure S13: (a) Graphical representation of $\delta^{51}V$ and $\delta^{88}Sr$ isotopic co-variations as a function of condensation (orange) and evaporation (green), considering that the fractions of V and Sr condensed or evaporated remain identical. Percentages associated with condensation and evaporation respectively correspond to the condensed and evaporated fractions (f) of V and Sr. The composition of the starting gas is assumed chondritic (**34**). **(b)** Comparing the $\delta^{51}V$- $\delta^{88}Sr$ composition of CAIs with condensation (orange) and evaporation (green) lines considering that the fractions of V and Sr condensed or evaporated remain identical (i.e., V and Sr have identical volatilities). We observe that the slope of the CAI correlation is markedly shallower than the pathways predicted by kinetic isotopic fractionation theory. Adjusting the slope of these theoretical lines to fit that of the CAI correlation is achieved by invoking distinct sticking coefficient ratios for the isotopes of Sr and V (e.g., $\gamma_{^{50}V} = \gamma_{^{51}V}$ and $\gamma_{^{86}Sr} = 0.9976 \times \gamma_{^{88}Sr}$; dashed line noted $f_\alpha{}'$). However, in this case, the predicted (dashed line) and observed (CAI correlation) lines are vertically shifted one from another, requiring the reservoir from which chondrites formed to have been enriched in ^{50}V with respect to that from which CAI condensed. The chondritic (black diamond) and BSE (black square) compositions are shown (**34**). The BSE is clearly distinct from the chondritic composition, but close to the CAI correlation.

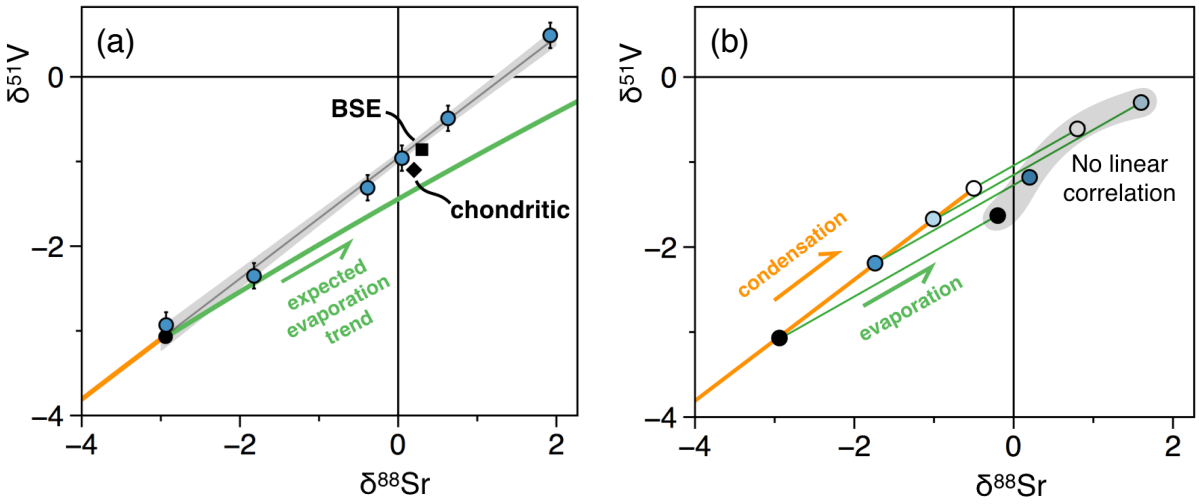

Figure S14: Testing the relationship between $f_{condensate}(V)$ and $f_{condensate}(Sr)$ for different scenarios of condensation/evaporation. The expected evaporation trend (green line) based on the same $f_{condensate}(V)$ - $f_{condensate}(Sr)$ relationship as derived from condensation is markedly different from the CAI correlation line **(a)**. One possibility is that the slope of the CAI correlation only reflects isotopic fractionation during evaporation. However, this would require all CAIs to have initially condensed to the exact same extent as, otherwise, no linear correlation would be expected for residues having experienced different extents of partial evaporation **(b)**. Another possibility is that the $f_{condensate}(V)$ - $f_{condensate}(Sr)$ relationships were different during condensation and evaporation (e.g., different sticking coefficients), producing condensation and evaporation trends that were roughly collinear and so unresolved at the current level of precision. The chondritic (black square) and BSE (black diamond) compositions are shown (**34**).

S9) Numerical Modeling of cosmogenic ^{10}Be and ^{50}V production

Numerical Modeling of cosmogenic ^{10}Be and ^{50}V production was carried out from the Matlab code developed by Liu and McKeegan (**69**). In an irradiation environment, the production of a nuclide P_j from spallation nuclear reactions on a target follows the equation

$$P_j = \sum_k \sum_i \int_0^T \int_E f_k(E,t)\, \sigma_{i\to j}(E)\, N_i\, dE\, dt \qquad \text{(Eq. S4)}$$

where $f_k(E,t)$ is the time dependent flux of various incoming particles, usually represented by a power-law distribution as a function of kinetic energy, $\sigma_{i\to j}(E)$ represents the cross section of a given nuclear reaction that converts a target nuclide "i" to a product isotope "j," and N_i is the number of atoms for target nuclide "i" per gram of sample material. The summation accounts for multiple species of projectiles "k" participating in the irradiation, and if more than one target is involved to produce "j", the contribution from each target isotope "i" has to be included (see, e.g., **3,13,20,21,69**).

The integrations over energy and over time yield P_j, the total production of nuclide "j" per gram. The relevant cross sections are obtained from the TALYS code (**68**), which calculates cross sections based on the Hauser–Feshbach statistical model. The calculations for both stable isotopes and radionuclides are performed by expressing the flux of projectiles in the form of a differential spectrum $\frac{dN}{dN} \propto E^{-p}$ with respect to kinetic energy, where the index p determines the steepness of the spectrum and also implies the constituents of the incident particles. For example, impulsive solar flare events are characterized by a steep energy spectrum with high p (=3.5) and high abundances of ^{3}He (^{3}He/^{4}He ~ 1), whereas gradual flares are described by a shallower spectral index (p = 2.7) and lower ^{3}He abundances (^{3}He/^{4}He ~ 4 x10^{-4}; **134**). Here, we adopt the proton flux estimated by Lee et al. (**20**) based upon the X-ray observations of embedded young solar-type stars (e.g., **135,136**), with F_p (E≥10 MeV) = 1.9 x 10^{10} cm^{-2}.s^{-1}.

For the ^{10}Be production calculations, the measured cross sections of ^{16}O(p,x)^{10}Be and ^{16}O(α,x)^{10}Be are adopted from Sisterson et al. (**67**) and Lange et al. (**137**), respectively. Contributions from ^{17}O(p,x)^{10}Be and ^{18}O(p,x)^{10}Be are considered negligible due to the low abundances of ^{17}O and ^{18}O. For the ^{50}V production calculations, we considered the reactions ^{50}Ti(p,n) ^{50}V, ^{52}Cr(p,2pn) ^{50}V, ^{48}Ti(α,αpn) ^{50}V, ^{51}V(p,2n) ^{50}V, ^{48}Ti(h,p) ^{50}V, ^{49}Ti(h,pn) ^{50}V, ^{50}Ti(h,p2n) ^{50}V, ^{52}Cr(p,2p) ^{51}V and ^{48}Ti(α,αp) ^{51}V. Although V production from ^{56}Fe target is usually not considered in the case of in-situ irradiation of proto-CAIs given that most (if not all) of ^{56}Fe in CAIs has a secondary origin (e.g., aqueous alteration), the reactions ^{56}Fe(p,x) ^{50}V and ^{56}Fe(p,x) ^{51}V were included here in the case of irradiation of nebular gas. The production rates of ^{10}Be and ^{50}V were calculated for the own chemical composition of each CAI (in the case of in-situ irradiation) and from the composition of bulk CI chondrites in the case of solar gas irradiation (**33**).

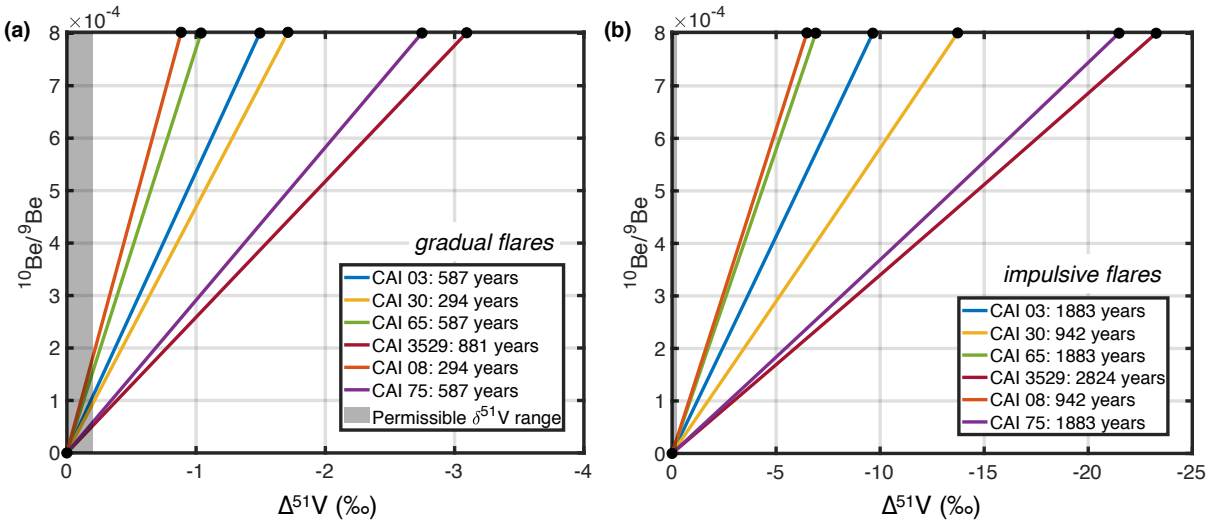

Figure S15: 2D projections of Figure 6, panels (a) and (b), in $\Delta^{51}V$-$^{10}Be/^{9}Be$ space (times of irradiation provided in the caption). Coloured lines correspond to the trajectories of proto-CAIs experiencing *in-situ* irradiation at 0.1 AU by gradual (a) and impulsive (b) flares. The different trajectories of CAIs, which all reach the canonical $^{10}Be/^{9}Be$ of ~8×10^{-4}, are controlled by their distinct abundances of target elements for cosmogenic production.

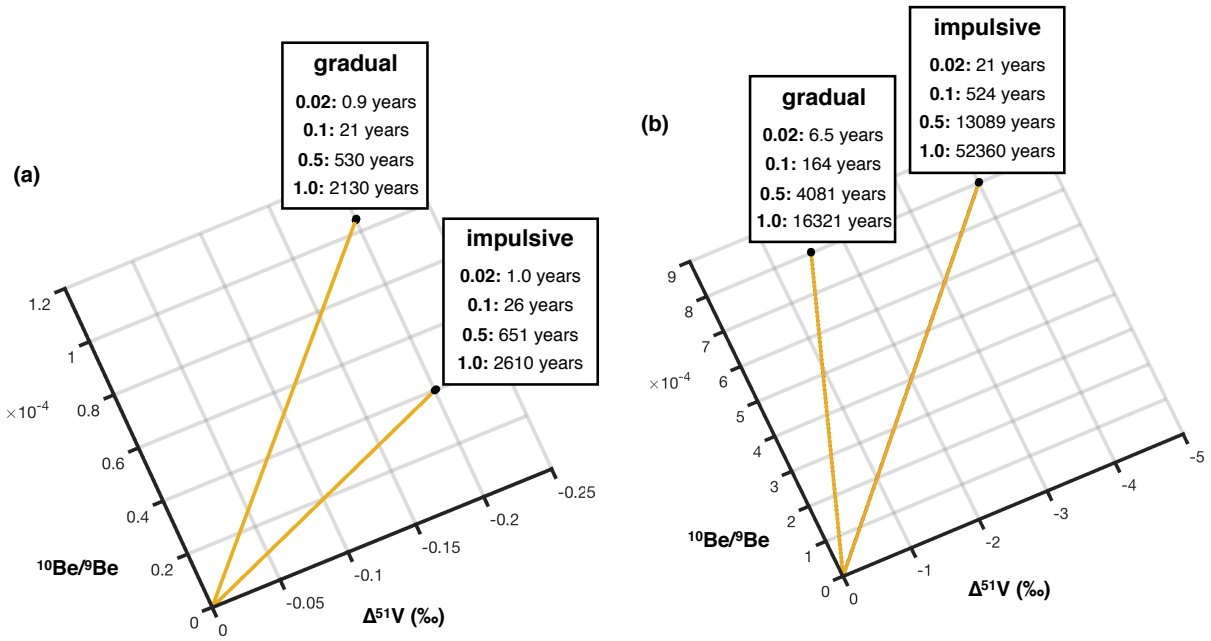

Figure S16: 2D projections of Figure 7 in $\Delta^{51}V$ -$^{10}Be/^{9}Be$ space, in the case of irradiation of solar gas at 0.02 AU, 0.1 AU, 0.5 AU, and 1.0 AU by gradual and impulsive flares. Panel (a) shows the expected $^{10}Be/^{9}Be$ variations associated with $\delta^{51}V$ values of ~0.2 ‰. Panel (b) shows the expected $\Delta^{51}V$ variations associated with a canonical $^{10}Be/^{9}Be$ of ~8×10^{-4}.

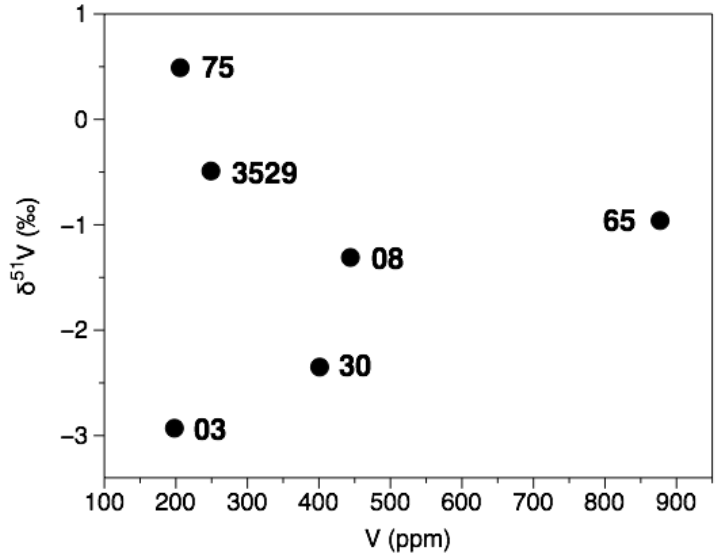

Figure S17: $\delta^{51}V$ versus V concentration of CAIs belonging to the $\delta^{51}V$-$\delta^{88}Sr$ correlation, showing the absence of correspondence between the concentration and isotope composition of V, as yet expected in the framework of evaporation/condensation from a common reservoir (**21**). This potentially suggests that the CAI factory did not possess a homogeneous reservoir with respect to V (see main text).

REFERENCES AND NOTES

1. S. J. Wolk, F. R. Harnden Jr, E. Flaccomio, G. Micela, F. Favata, H. Shang, E. D. Feigelson, Stellar activity on the young suns of Orion: COUP observations of K5-7 pre-main-sequence stars. *Astrophys. J. Suppl. Ser.* **160**, 423–449 (2005).

2. C. Ceccarelli, C. Dominik, A. López-Sepulcre, M. Kama, M. Padovani, E. Caux, P. Caselli, HERSCHELFINDS evidence for stellar wind particles in a protostellar envelope: Is this what happened to the young sun? *Astrophys. J. Lett.* **790**, L1 (2014).

3. M. Gounelle, F. H. Shu, H. Shang, A. E. Glassgold, K. E. Rehm, T. Lee, Extinct radioactivities and protosolar cosmic rays: Self-shielding and light elements. *Astrophys. J.* **548**, 1051–1070 (2001).

4. J. Chmeleff, F. von Blanckenburg, K. Kossert, D. Jakob, Determination of the ^{10}Be half-life by multicollector ICP-MS and liquid scintillation counting. *Nucl. Instrum. Methods Phys. Res. Sect. B* **268**, 192–199 (2010).

5. K. D. McKeegan, M. Chaussidon, F. Robert, Incorporation of short-lived ^{10}Be in a calcium-aluminum-rich inclusion from the Allende meteorite. *Science* **289**, 1334–1337 (2000).

6. N. Sugiura, Y. Shuzou, A. Ulyanov, Beryllium-boron and aluminum-magnesium chronology of calcium-aluminum-rich inclusions in CV chondrites. *Meteorit. Planet. Sci.* **36**, 1397–1408 (2001).

7. G. J. MacPherson, G. R. Huss, A. M. Davis, Extinct ^{10}Be in type A calcium-aluminum-rich inclusions from CV chondrites. *Geochim. Cosmochim. Acta* **67**, 3165–3179 (2003).

8. M. Chaussidon, F. Robert, K. D. McKeegan, Li and B isotopic variations in an Allende CAI: Evidence for the in situ decay of short-lived ^{10}Be and for the possible presence of the short-lived nuclide ^{7}Be in the early solar system. *Geochim. Cosmochim. Acta* **70**, 224–245 (2006).

9. D. Wielandt, K. Nagashima, A. N. Krot, G. R. Huss, M. A. Ivanova, M. Bizzarro, Evidence for multiple sources of ^{10}Be in the early solar system. *Astrophys. J. Lett.* **748**, L25 (2012).

10. G. Srinivasan, M. Chaussidon, Constraints on ^{10}Be and ^{41}Ca distribution in the early solar system from ^{26}Al and ^{10}Be studies of Efremovka CAIs. *Earth Planet. Sci. Lett.* **374**, 11–23 (2013).

11. S. J. Desch, H. C. Connolly Jr, G. Srinivasan, An interstellar origin for the beryllium 10 in calcium-rich, aluminum-rich inclusions. *Astrophys. J.* **602**, 528–542 (2004).

12. V. Tatischeff, J. Duprat, N. De Séréville, Light-element nucleosynthesis in a molecular cloud interacting with a supernova remnant and the origin of beryllium-10 in the protosolar nebula. *Astrophys. J.* **796**, 124 (2014).

13. I. Leya, A. N. Halliday, R. Wieler, The predictable collateral consequences of nucleosynthesis by spallation reactions in the early solar system. *Astrophys. J.* **594**, 605–616 (2003).

14. G. J. MacPherson, Calcium-aluminum-rich inclusions in chondritic meteorites. *Treatise Geochem.* **1**, 711 (2003).

15. F. M. Richter, P. E. Janney, R. A. Mendybaev, A. M. Davis, M. Wadhwa, Elemental and isotopic fractionation of Type B CAI-like liquids by evaporation. *Geochim. Cosmochim. Acta* **71**, 5544–5564 (2007).

16. D. S. Ebel, Condensation of rocky material in astrophysical environments. *Meteorites Early Solar Syst. II* **1**, 253–277 (2006).

17. Y. Amelin, A. Kaltenbach, T. Iizuka, C. H. Stirling, T. R. Ireland, M. Petaev, S. B. Jacobsen, U–Pb chronology of the Solar System's oldest solids with variable $^{238}U/^{235}U$. *Earth Planet. Sci. Lett.* **300**, 343–350 (2010).

18. A. Bouvier, G. A. Brennecka, M. Wadhwa, Absolute chronology of the first solids in the Solar System. *LPICo* **1639**, 9054 (2011).

19. J. N. Connelly, M. Bizzarro, A. N. Krot, Å. Nordlund, D. Wielandt, M. A. Ivanova, The absolute chronology and thermal processing of solids in the solar protoplanetary disk. *Science* **338**, 651–655 (2012).

20. T. Lee, F. H. Shu, H. Shang, A. E. Glassgold, K. E. Rehm, Protostellar cosmic rays and extinct radioactivities in meteorites. *Astrophys. J.* **506**, 898–912 (1998).

21. P. A. Sossi, F. Moynier, M. Chaussidon, J. Villeneuve, C. Kato, M. Gounelle, Early Solar System irradiation quantified by linked vanadium and beryllium isotope variations in meteorites. *Nat. Astron.* **1**, 0055 (2017).

22. P. H. Warren, Stable-isotopic anomalies and the accretionary assemblage of the Earth and Mars: A subordinate role for carbonaceous chondrites. *Earth Planet. Sci. Lett.* **311**, 93–100 (2011).

23. T. S. Kruijer, C. Burkhardt, G. Budde, T. Kleine, Age of Jupiter inferred from the distinct genetics and formation times of meteorites. *Proc. Natl. Acad. Sci. U.S.A.* **114**, 6712–6716 (2017).

24. S. J. Desch, A. Kalyaan, C. M. D. Alexander, The effect of Jupiter's formation on the distribution of refractory elements and inclusions in meteorites. *Astrophys. J. Suppl. Ser.* **238**, 11 (2018).

25. T. Haugbølle, P. Weber, D. P. Wielandt, P. Benítez-Llambay, M. Bizzarro, O. Gressel, M. E. Pessah, Probing the protosolar disk using dust filtering at gaps in the early solar system. *Astronom. J.* **158**, 55 (2019).

26. L. Yang, F. J. Ciesla, The effects of disk building on the distributions of refractory materials in the solar nebula. *Meteoritics Planet. Sci.* **47**, 99–119 (2012).

27. L. Grossman, S. B. Simon, V. K. Rai, M. H. Thiemens, I. D. Hutcheon, R. W. Williams, A. Galy, T. Ding, A. V. Fedkin, R. N. Clayton, T. K. Mayeda, Primordial compositions of refractory inclusions. *Geochim. Cosmochim. Acta* **72**, 3001–3021 (2008).

28. J. Render, G. A. Brennecka, S. J. Wang, L. E. Wasylenki, T. Kleine, A distinct nucleosynthetic heritage for early solar system solids recorded by Ni isotope signatures. *Astrophys. J.* **862**, 26 (2018).

29. K. R. Bermingham, N. Gussone, K. Mezger, J. Krause, Origins of mass-dependent and mass-independent Ca isotope variations in meteoritic components and meteorites. *Geochim. Cosmochim. Acta* **226**, 206–223 (2018).

30. A. M. Davis, J. Zhang, N. D. Greber, J. Hu, F. L. Tissot, N. Dauphas, Titanium isotopes and rare earth patterns in CAIs: Evidence for thermal processing and gas-dust decoupling in the protoplanetary disk. *Geochim. Cosmochim. Acta* **221**, 275–295 (2018).

31. B. L. A. Charlier, F. L. H. Tissot, N. Dauphas, C. J. N. Wilson, Nucleosynthetic, radiogenic and stable strontium isotopic variations in fine- and coarse-grained refractory inclusions from Allende. *Geochim. Cosmochim. Acta* **265**, 413–430 (2019).

32. Q. R. Shollenberger, A. Wittke, J. Render, P. Mane, S. Schuth, S. Weyer, N. Gusson, M. Wadhw, G. A. Brennecka, Combined mass-dependent and nucleosynthetic isotope variations in refractory inclusions and their mineral separates to determine their original Fe isotope compositions. *Geochim. Cosmochim. Acta* **263**, 215–234 (2019).

33. K. Lodders, Solar system abundances and condensation temperatures of the elements. *Astrophys. J.* **591**, 1220–1247 (2003).

34. S. G. Nielsen, D. Bekaert, T. Magna, K. Mezger, M. Auro, The vanadium isotope composition of Mars: Implications for planetary differentiation in the early solar system. *Geochem. Perspect. Lett.* **15**, 35–39 (2020).

35. P. J. Patchett, Sr isotopic fractionation in Ca–Al inclusions from the Allende meteorite. *Nature* **283**, 438–441 (1980).

36. T. R. Ireland, B. Fegley Jr., The solar system's earliest chemistry: Systematics of refractory inclusions. *Int. Geol. Rev.* **42**, 865–894 (2000).

37. W. V. Boynton, Fractionation in the solar nebula: Condensation of yttrium and the rare earth elements. *Geochim. Cosmochim. Acta* **39,** 569–584 (1975).

38. E. T. Dunham, M. Wadhwa, S. J.Desch, R. L. Hervig, Best practices for determination of Initial $^{10}Be/^{9}Be$ in early solar system materials by secondary ion mass spectrometry. *Geostand. Geoanal. Res.* **44**, 695–710 (2020).

39. E. Rotenberg, D. W. Davis, Y. Amelin, S. Ghosh, B. A. Bergquist, Determination of the decay-constant of ^{87}Rb by laboratory accumulation of ^{87}Sr. *Geochim. Cosmochim. Acta* **85**, 41–57 (2012).

40. F. Moynier, J. I. Simon, F. A. Podosek, B. S. Meyer, J. Brannon, D. J. DePaolo, Ca isotope effects in Orgueil leachates and the implications for the carrier phases of ^{54}Cr anomalies. *Astrophys. J. Lett.* **718**, L7–L13 (2010).

41. B.L.A. Charlier, G.M. Nowell, I.J. Parkinson, S.P. Kelley, D.G. Pearson, K.W. Burton, High temperature strontium stable isotope behaviour in the early solar system and planetary bodies. *Earth Planet. Sci. Lett.* **329**, 31–40 (2012).

42. D. A. H. Teagle, M. J. Bickle, J. C. Alt, Recharge flux to ocean-ridge black smoker systems: A geochemical estimate from ODP Hole 504B. *Earth Planet. Sci. Lett.* **210**, 81–89 (2003).

43. J. Prytulak, S. G. Nielsen, D. A. Ionov, A. N. Halliday, J. Harvey, K. A. Kelley, Y. L. Niu, D. W. Peate, K. Shimizu. K. W. W. Sims, The stable vanadium isotope composition of the mantle and mafic lavas. *Earth Planet. Sci. Lett.* **365**, 177–189 (2013).

44. J. Pape, K. Mezger, A. S. Bouvier, L. P. Baumgartner, Time and duration of chondrule formation: Constraints from ^{26}Al-^{26}Mg ages of individual chondrules. *Geochim. Cosmochim. Acta* **244**, 416–436 (2019).

45. J. Bollard, J. N. Connelly, M. J. Whitehouse, E. A. Pringle, L. Bonal, J. K. Jørgensen, Å. Nordlund, F. Moynier, M. Bizzarro, Early formation of planetary building blocks inferred from Pb isotopic ages of chondrules. *Sci. Adv.* **3**, e1700407 (2017).

46. C. Burkhardt, N. Dauphas, U. Hans, B. Bourdon, T. Kleine, Elemental and isotopic variability in solar system materials by mixing and processing of primordial disk reservoirs. *Geochim. Cosmochim. Acta* **261**, 145–170 (2019).

47. J. A. M. Nanne, F. Nimmo, J. N. Cuzzi, T. Kleine, Origin of the non-carbonaceous–carbonaceous meteorite dichotomy. *Earth Planet. Sci. Lett.* **511**, 44–54 (2019).

48. S. G. Nielsen, M. Auro, K. Righter, D. Davis, J. Prytulak, F. Wu, J. D. Owens, Nucleosynthetic vanadium isotope heterogeneity of the early solar system recorded in chondritic meteorites. *Earth Planet. Sci. Lett.* **505**, 131–140 (2019).

49. S. S. Hopkins, J. Prytulak, J. Barling, S. S. Russell, B. J. Coles, A. N. Halliday, The vanadium isotopic composition of lunar basalts. *Earth Planet. Sci. Lett.* **511**, 12–24 (2019).

50. D. Clayton, *Handbook of Isotopes in the Cosmos: Hydrogen to Gallium* (Cambridge Univ. Press, 2003), vol. 1.

51. E. A. Schauble, First-principles estimates of equilibrium magnesium isotope fractionation in silicate, oxide, carbonate and hexaaquamagnesium(2+) crystals. *Geochim. Cosmochim. Acta* **75**, 844–869 (2011).

52. J. I. Simon, M. K. Jordan, M. J. Tappa, E. A. Schauble, I. E. Kohl, E. D. Young, Calcium and titanium isotope fractionation in refractory inclusions: Tracers of condensation and inheritance in the early solar protoplanetary disk. *Earth Planet. Sci. Lett.* **472**, 277–288 (2017).

53. P. A. Sossi, B. Fegley Jr, Thermodynamics of element volatility and its application to planetary processes. *Rev. Mineral. Geochem.* **84**, 393–459 (2018).

54. F. M. Richter, Timescales determining the degree of kinetic isotope fractionation by evaporation and condensation. *Geochim. Cosmochim. Acta* **68**, 4971–4992 (2004).

55. J. P. Hirth, G. M. Pound, Coefficients of condensation, evaporation and thermal accommodation. *Prog. Mater. Sci.* **11**, 1 (1963).

56. D. S. Ebel, L. Grossman, Condensation in dust-enriched systems. *Geochim. Cosmochim. Acta* **64**, 339–366 (2000).

57. B. J. Wood, D. J. Smythe, T. Harrison, The condensation temperatures of the elements: A reappraisal. *Am. Mineral. J. Earth Planet. Mater.* **104**, 844–856 (2019).

58. B. Fegley Jr, H. Palme, Evidence for oxidizing conditions in the solar nebula from Mo and W depletions in refractory inclusions in carbonaceous chondrites. *Earth Planet. Sci. Lett.* **72**, 311–326 (1985).

59. A. S. Kornacki, B. Fegley Jr, The abundance and relative volatility of refractory trace elements in Allende Ca,Al-rich inclusions: Implications for chemical and physical processes in the solar nebula. *Earth Planet. Sci. Lett.* **79**, 217–234 (1986).

60. A. M. Davis, L. Grossman, Condensation and fractionation of rare earths in the solar nebula. *Geochim. Cosmochim. Acta* **43**, 1611–1632 (1979).

61. J. Y. Hu, N. Dauphas, F. L. H. Tissot, R. Yokochi, T. J. Ireland, Z. Zhang, A. M. Davis, F. J. Ciesla, L. Grossman, B. L. A. Charlier, M. Roskosz, E. E. Alp, M. Y. Hu, J. Zhao, Heating events in the nascent solar system recorded by rare earth element isotopic fractionation in refractory inclusions. *Sci. Adv.* **7**, eabc2962 (2021).

62. F. R. Niederer, D. A. Papanastassiou, Ca isotopes in refractory inclusions. *Geochim. Cosmochim. Acta* **48**, 1279–1293 (1984).

63. S. Huang, J. Farkaš, G. Yu, M. I. Petaev, S. B. Jacobsen**,** Calcium isotopic ratios and rare earth element abundances in refractory inclusions from the Allende CV3 chondrite. *Geochim. Cosmochim. Acta* **77**, 252–265 (2012).

64. M. Gounelle, M. Chaussidon, C. Rollion-Bard, Variable and extreme irradiation conditions in the early solar system inferred from the initial abundance of ^{10}Be in Isheyevo CAIs. *Astrophys. J. Lett.* **763**, L33 (2013).

65. K. Fukuda, H. Hiyagon, W. Fujiya, N. Takahata, T. Kagoshima, Y. Sano, Origin of the short-lived radionuclide ^{10}Be and its implications for the astronomical setting of CAI formation in the solar protoplanetary disk. *Astrophys. J.* **886**, 34 (2019).

66. K. Fukuda, H. Hiyagon, W. Fujiya, T. Kagoshima, K. Itano, T. Iizuka, N. T. Kita, Y. Sano, Irradiation origin of ^{10}Be in the solar nebula: Evidence from Li-Be-B and Al-Mg isotope

systematics, and REE abundances of CAIs from Yamato-81020 CO3.05 chondrite. *Geochim. Cosmochim. Acta* **293**, 187–204 (2021).

67. J. M. Sisterson, K. Kim, A. Beverding, P. A. J. Englert, M. Caffee, A. T. Jull, D. J. Donahue, L. McHargue, C. Castaneda, J. Vincent, R. C. Reedy, Measurement of proton production cross sections of ^{10}Be and ^{26}Al from elements found in lunar rocks. *Nucl. Instrum. Methods Phys. Res., Sect. B* **123**, 324–329 (1997).

68. A. J. Koning, S. Hilaire, M. C. Duijvestijn, TALYS: Comprehensive Nuclear Reaction Modeling, in *Proceedings of the International Conference on Nuclear Data for Science and Technology (AIP Conf. Proc. 769)*, R. C. Haight, Ed. (AIP, 2005), p. 1154.

69. M. C. Liu, K. D. McKeegan, On an irradiation origin for magnesium isotope anomalies in meteoritic hibonite. *Astrophys. J. Lett.* **697**, L145–L148 (2009).

70. M.-C. Liu, L. R. Nittler, C. M. D. Alexander, T. Lee, Lithium–Beryllium–Boron isotopic compositions in meteoritic hibonite: Implications for origin of ^{10}Be and early Solar System irradiation. *Astrophys. J. Lett.* **719**, L99–L103 (2010).

71. N. Dauphas, M. Chaussidon, A perspective from extinct radionuclides on a young stellar object: The Sun and its accretion disk. *Annu. Rev. Earth Planet. Sci.* **39**, 351–386 (2011).

72. E. Jacquet, Beryllium-10 production in gaseous protoplanetary disks and implications for the astrophysical setting of refractory inclusions. *Astron. Astrophys.* **624**, A131 (2019).

73. N. Ouellette, S. J. Desch, M. Bizzarro, A. P. Boss, F. Ciesla, B. Meyer, Injection mechanisms of short-lived radionuclides and their homogenization. *Geochim. Cosmochim. Acta* **73**, 4946–4962 (2009).

74. K. K. Marhas, J. N. Goswami, A. M. Davis, Short-lived nuclides in hibonite grains from Murchison: Evidence for solar system evolution. *Science* **298**, 2182–2185 (2002).

75. M. C. Liu, K. D. McKeegan, J. N., K. K. Marhas, S. Sahijpal, T. R. Ireland, A. M. Davis, Isotopic records in CM hibonites: Implications for timescales of mixing of isotope reservoirs in the solar nebula. *Geochim. Cosmochim. Acta* **73**, 5051–5079 (2009).

76. G. J. MacPherson, E. S. Bullock, P. E. Janney, N. T. Kita, T. Ushikubo, A. M. Davis, M. Wadhwa A. N. Krot, Early solar nebula condensates with canonical, not supracanonical, initial $^{26}Al/^{27}Al$ ratios. *Astrophys. J. Lett.* **711**, L117–L121 (2010).

77. G. A. Brennecka, C. Burkhardt, G. Budde, T. S. Kruijer, F. Nimmo, T. Kleine, Astronomical context of Solar System formation from molybdenum isotopes in meteorite inclusions. *Science* **370**, 837–840 (2020).

78. M. Audard, P. Ábrahám, M. M. Dunham, J. D. Green, N. Grosso, K. Hamaguchi, J. H. Kastner, Á. Kóspál, G. Lodato, M. Romanova, S. L. Skinner, E. I. Vorobyov, Z. Zhu, Z. Zhu, Episodic accretion in young stars, in *Protostars and Planets VI*, H. Beuther, R. Klessen, C. Dullemond, Th. Henning, Eds. (University of Arizona Press, 2014), p. 387.

79. G. J. MacPherson, Once a CAI, always a CAI: Flare-up-induced episodic fractionation and melting in the Early Solar Nebula, in *Lunar and Planetary Science Conference* (Department of Mineral Sciences, Museum of Natural History, Smithsonian Institution, No. 1964, 2017), p. 2719.

80. K. K. Larsen, D. Wielandt, M. Schiller, A. N. Krot, M. Bizzarro, Episodic formation of refractory inclusions in the Solar System and their presolar heritage. *Earth Planet. Sci. Lett.* **535**, 116088 (2020).

81. F. H. Shu, H. Shang, M. Gounelle, A. E. Glassgold, T. Lee, The origin of chondrules and refractory inclusions in chondritic meteorites. *Astrophys. J.* **548**, 1029–1050 (2001).

82. R. Hueso, T. Guillot, Evolution of protoplanetary disks: Constraints from DM Tauri and GM Aurigae. *Astron. Astrophys.* **442**, 703–725 (2005).

83. C. P. Dullemond, D. Apai, S. Walch, Crystalline silicates as a probe of disk formation history. *Astrophys. J. Lett.* **640**, L67–L70 (2006).

84. F. C. Pignatale, S. Charnoz, M. Chaussidon, E. Jacquet, Making the planetary material diversity during the early assembling of the solar system. *Astrophys. J. Lett.* **867**, L23 (2018).

85. J. E. Lee, E. A. Bergin, J. R. Lyons, Oxygen isotope anomalies of the Sun and the original environment of the solar system. *Meteorit. Planet. Sci.* **43**, 1351–1362 (2008).

86. V. Agra-Amboage, C. Dougados, S. Cabrit, J. Reunanen, Sub-arcsecond [Fe ii] spectro-imaging of the DG Tauri jet-Periodic bubbles and a dusty disk wind?. *Astron. Astrophys.* **532**, A59 (2011).

87. R. K. Mishra, K. K. Marhas, Meteoritic evidence of a late superflare as source of ^{7}Be in the early Solar System. *Nat. Astron.* **3**, 498–505 (2019).

88. S. J. Desch, N. Ouellette, Comment on "Li and Be isotopic variations in an Allende CAI: Evidence for the in situ decay of short-lived ^{10}Be and for the possible presence of the short-lived nuclide ^{7}Be in the early solar system," by M. Chaussidon, F. Robert, and KD McKeegan. *Geochim. Cosmochim. Acta* **70**, 5426–5432 (2006).

89. L. Kööp, P. R. Heck, H. Busemann, A. M. Davis, J. Greer, C. Maden, M. M. M. Meier, R. Wieler, High early solar activity inferred from helium and neon excesses in the oldest meteorite inclusions. *Nat. Astron.* **2**, 709–713 (2018).

90. D. York, N. M. Evensen, M. L. Martinez, J. De Basabe Delgado, Unified equations for the slope, intercept, and standard errors of the best straight line. *Am. J. Phys.* **72**, 367–375 (2004).

91. M. Zhai, E. Nakamura, D. M. Shaw, T. Nakano, Boron isotope ratios in meteorites and lunar rocks. *Geochim. Cosmochim. Acta* **60**, 4877–4881 (1996).

92. S. G. Nielsen, J. Prytulak, A. N. Halliday, Determination of precise and accurate ^{51}V/^{50}V isotope ratios by MC-ICP-MS, Part 1: Chemical separation of vanadium and mass spectrometric protocols. *Geostand. Geoanal. Res.* **35**, 293–306 (2011).

93. F. Wu, Y. Qi, H. Yu, S. Tian, Z. Hou, F. Huang, Vanadium isotope measurement by MC-ICP-MS. *Chem. Geol.* **421**, 17–25 (2016).

94. J. Prytulak, P. A. Sossi, A. N. Halliday, T. Plank, P. S. Savage, J. D. Woodhead, Stable vanadium isotopes as a redox proxy in magmatic systems?. *Geochem. Perspect. Lett.* **3**, 75–84 (2016).

95. F. Wu, J. D. Owens, T. Huang, A. Sarafian, K. F. Huang, I. S. Sen, T. J. Horner, J. Blusztajn, P. Morton, S. G. Nielsen, Vanadium isotope composition of seawater. *Geochim. Cosmochim. Acta* **244**, 403–415 (2019).

96. S. Schuth, I. Horn, A. Brüske, P. E. Wolff, S. Weyer, First vanadium isotope analyses of V-rich minerals by femtosecond laser ablation and solution-nebulization MC-ICP-MS. *Ore Geol. Rev.* **81**, 1271–1286 (2017).

97. S. G. Nielsen, D. V. Bekaert, M. Auro Isotopic evidence for the formation of the Moon in a canonical giant impact. *Nat. Commun.* **12**, 1817 (2021).

98. S. G. Nielsen, J. D. Owens, T. J. Horner, Analysis of high-precision vanadium isotope ratios by medium resolution MC-ICP-MS. *J. Anal. At. Spectrom.* **31**, 531–536 (2016).

99. J. Prytulak, S. G. Nielsen, A. N. Halliday, Determination of precise and accurate $^{51}V/^{50}V$ Isotope ratios by multi-collector ICP-MS, Part 2: Isotopic composition of six reference materials plus the allende chondrite and verification tests. *Geostand. Geoanal. Res.* **35**, 307–318 (2011).

100. F. Wu, Y. Qi, M. R. Perfit, Y. Gao, C. H. Langmuir, V. D. Wanless, H. Yu, F. Huang, Vanadium isotope compositions of mid-ocean ridge lavas and altered oceanic crust. *Earth Planet. Sci. Lett.* **493**, 128–139 (2018).

101. B. L. A. Charlier, I. J. Parkinson, K. W. Burton, M. M. Grady, C. J. N. Wilson, E. G. C. Smith, Stable strontium isotopic heterogeneity in the solar system from double-spike data. *Geochem. Persp. Lett.* **4**, 35–40 (2017).

102. C. Deniel, C. Pin, Single-stage method for the simultaneous isolation of lead and strontium from silicate samples for isotopic measurements. *Anal. Chim. Acta* **426**, 95–103 (2001).

103. F. Albarède, B. Beard, Analytical methods for non-traditional isotopes, in *Reviews in Mineralogy and Geochemistry*, J. J. Rosso, Ed. (Mineralogical Society of America, 2004), pp. 113–152.

104. H. R. Marschall, B. D. Monteleone, Boron isotope analysis of silicate glass with very low boron concentrations by secondary ion mass spectrometry. *Geostand. Geoanal. Res.* **39**, 31–46 (2015).

105. H. R. Marschall, T. Ludwig, The Low-Boron contest: Minimising surface contamination and analysing boron concentrations at the ng/g-level by secondary ion mass spectrometry. *Mineral. Petrol.* **81**, 265–278 (2004).

106. T. Ludwig, H. R. Marschall, P. A. E. Pogge von Strandmann, B. M. Shabaga, M. Fayek, F. C. Hawthorne, A secondary ion mass spectrometry (SIMS) re-evaluation of B and Li isotopic compositions of Cu-bearing elbaite from three global localities. *Mineral. Mag.* **75**, 2485–2494 (2011)

107. R. C. Ogliore, G. R. Huss, K. Nagashima, Ratio estimation in SIMS analysis. *Nucl. Instrum. Methods Phys. Res. B* **269**, 1910–1918 (2011).

108. M.-C. Liu, J. Han, A. J. Brearley, A. T. Hertwig, Aluminum-26 chronology of dust coagulation and early solar system evolution. *Sci. Adv.* **5**, eaaw3350 (2019).

109. T. Gregory, T. H. Luu, C. D. Coath, S. S. Russell, T. Elliott, Primordial formation of major silicates in a protoplanetary disc with homogeneous $^{26}Al/^{27}Al$. *Sci. Adv.* **6**, eaay9626 (2020).

110. B. Jacobsen, Q. Z. Yin, F. Moynier, Y. Amelin, A. N. Krot, K. Nagashima, I. D. Hutcheon, H. Palme, ^{26}Al–^{26}Mg and ^{207}Pb–^{206}Pb systematics of Allende CAIs: Canonical solar initial $^{26}Al/^{27}Al$ ratio reinstated. *Earth Planet. Sci. Lett.* **272**, 353–364 (2008).

111. N. T. Kita, Q. Z. Yin, G. J. MacPherson, T. Ushikubo, B. Jacobsen, K. Nagashima, E. Kurahashi, A. N. Krot, S. B. Jacobsen, ^{26}Al-^{26}Mg isotope systematics of the first solids in the early solar system. *Meteorit. Planet. Sci.* **48**, 1383–1400 (2013).

112. K. P. Jochum, D. B. Dingwell, A. Rocholl, B. Stoll, A. W. Hofmann, S. Becker, A. Besmehn, D. Bessette, H.-J. Dietze, P. Dulski, J. Erzinger, E. Hellebrand, P. Hoppe, I. Horn, K. Janssens, G.A. Jenner, M. Klein, W.F. Mc Donough, M. Maetz, K. Mezger, C. Müker, I.K. Nikogosian, C. Pickhardt, I. Raczek, D. Rhede, H. M. Seufert, S.G. Simakin, A.V. Sobolev, B. Spettel, S. Straub, L. Vincze, A. Wallianos, G. Weckwerth, S. Weyer, D. Wolf, M. Zimmer, The preparation and

preliminary characterisation of eight geological MPI-DING reference glasses for in-situ microanalysis. *Geostand. Newsl.* **24**, 87–133 (2000)

113. K. P. Jochum, B. Stoll, K. Herwig, M. Willbold, A. W. Hofmann, M. Amini, S. Aarburg, W. Abouchami, E. Hellebrand, B. Mocek, I. Raczek, A. Stracke, O. Alard, C. Bouman, S. Becker, M. Dücking, H. Brätz, R. Klemd, D. de Bruin, D. Canil, D. Cornell, Cees-Jan de Hoog, C. Dalpé, L. Danyushevsky, A. Eisenhauer, Y. Gao, J. E. Snow, N. Groschopf, D. Günther, C. Latkoczy, M. Guillong, E. H. Hauri, H. E. Höfer, Y. Lahaye, K. Horz, D. E. Jacob, S. A. Kasemann, A. J. R. Kent, T. Ludwig, T. Zack, P. R. D. Mason, A. Meixner, M. Rosner, K. Misawa, B. P. Nash, J. Pfänder, W. R. Premo, W. D. Sun, M. Tiepolo, R. Vannucci, T. Vennemann, D. Wayne, J. D. Woodhead, MPI-DING reference glasses for in situ microanalysis: New reference values for element concentrations and isotope ratios. *Geochem. Geophys. Geosyst.* **7**, Q02008 (2006).

114. D. M. Shaw, M. D. Higgins, M. G. Truscott, T. A. Middleton, Boron contamination in polished thin sections of meteorites: Implications for other trace-element studies by alpha-track image or ion microprobe. *Am. Mineral.* **73**, 894–900 (1988).

115. M. Chaussidon, F. Robert, D. Mangin, P. Hanon, E. F. Rose, Analytical procedures for the measurement of boron isotope compositions by ion microprobe in meteorites and mantle rocks. *Geostand. Newslett.* **21**, 7–17 (1997).

116. T. Nakano, E. Nakamura, Boron isotope geochemistry of metasedimentary rocks and tourmalines in a subduction zone metamorphic suite. *Phys. Earth Planet. In.* **127**, 233–252 (2001).

117. M. Rosner, M. Wiedenbeck, T. Ludwig, Composition-induced variations in SIMS instrumental mass fractionation during boron isotope ratio measurements of silicate glasses. *Geostand. Geoanal. Res.* **32**, 27–38 (2008).

118. A. A. Gurenko, V. S. Kamenetsky, Boron isotopic composition of olivine-hosted melt inclusions from Gorgona komatiites, Colombia: New evidence supporting wet komatiite origin. *Earth Planet. Sci. Lett.* **312**, 201–212 (2011).

119. S. Pabst, T. Zack, I. P. Savov, T. Ludwig, D. Rost, S. Tonarini, E. P. Vicenzi, The fate of subducted oceanic slabs in the shallow mantle: Insights from boron isotopes and light element composition of metasomatized blueschists from the Mariana forearc. *Lithos* **132-133**, 162–179 (2012).

120. Q. R. Shollenberger, G. A. Brennecka, Dy, Er, and Yb isotope compositions of meteorites and their components: Constraints on presolar carriers of the rare earth elements. *Earth Planet. Sci. Lett.* **529**, 115866 (2020).

121. M. Rotaru, J. L. Birck, C. J. Allègre, Clues to early solar system history from chromium isotopes in carbonaceous chondrites. *Nature* **358**, 465–470 (1992).

122. F. A. Podosek, U. Ott, J. C. Brannon, C. R. Neal, T. J. Bernatowicz, P. Swan, S. E. Mahan, Thoroughly anomalous chromium in Orgueil. *Meteorit. Planet. Sci.* **32**, 617–627 (1997).

123. N. Dauphas, B. Marty, L. Reisberg, Molybdenum nucleosynthetic dichotomy revealed in primitive meteorites. *Astrophys. J. Lett.* **569**, L139–L142 (2002).

124. H. Hidaka, S. Yoneda, Diverse nucleosynthetic components in barium isotopes of carbonaceous chondrites: Incomplete mixing of s- and r-process isotopes and extinct ^{135}Cs in the early solar system. *Geochim. Cosmochim. Acta* **75**, 3687–3697 (2011).

125. M. Schönbächler, M. Rehkämper, M. A. Fehr, A. N. Halliday, B. Hattendorf, D. Günther, Nucleosynthetic zirconium isotope anomalies in acid leachates of carbonaceous chondrites. *Geochim. Cosmochim. Acta* **69**, 5113–5122 (2005).

126. T. Yokoyama, C. M. D. Alexander, M. Conel, R. J. Walker, Osmium isotope anomalies in chondrites: Results for acid residues and related leachates. *Earth Planet. Sci. Lett.* **291**, 48–59 (2010).

127. T. Yokoyama, Y. Fukami, W. Okui, N. Ito, H. Yamazaki, Nucleosynthetic strontium isotope anomalies in carbonaceous chondrites. *Earth Planet. Sci. Lett.* **416**, 46–55 (2015).

128. L. Reisberg, N. Dauphas, A. Dauphas, D. G. Pearson, R. Gallino, C. Zimmermann, Nucleosynthetic osmium isotope anomalies in acid leachates of the Murchison meteorite. *Earth Planet. Sci. Lett.* **277**, 334–344 (2009).

129. F. Moynier, A. Agranier, D. C. Hezel, A. Bouvier, Sr stable isotope composition of Earth, the Moon, Mars, Vesta and meteorites. *Earth Planet. Sci. Lett.* **300**, 359–366 (2010).

130. L. Qin, R. W. Carlson, C. M. D. Alexander Correlated nucleosynthetic isotopic variability in Cr, Sr, Ba, Sm, Nd and Hf in Murchison and QUE 97008. *Geochim. Cosmochim. Acta* **75**, 7806–7828 (2011).

131. C. Burkhardt, T. Kleine, N. Dauphas, R. Wieler, Nucleosynthetic tungsten isotope anomalies in acid leachates of the Murchison chondrite: Implications for hafnium-tungsten chronometry. *Astrophys. J. Lett.* **753**, L6 (2012).

132. C. Burkhardt, M. Schönbächler, Intrinsic W nucleosynthetic isotope variations in carbonaceous chondrites: Implications for W nucleosynthesis and nebular vs. parent body processing of presolar materials. *Geochim. Cosmochim. Acta* **165**, 361–375 (2015).

133. M. Fischer-Gödde, C. Burkhardt, T. S. Kruijer, T. Kleine, Ru isotope heterogeneity in the solar protoplanetary disk. *Geochim. Cosmochim. Acta* **168**, 151–171 (2015).

134. M. Desai, J. Giacalone, Large gradual solar energetic particle events. *Living Rev. Sol. Phys.* **13**, 3 (2016).

135. Y. Kamata, K. Koyama, Y. Tsuboi, S. Yamauchi, X-ray analysis of the ρ Ophiuchi dark cloud with ASCA: Source identification, X-ray spectra, and temporal variability. *Publ. Astron. Soc. Jpn.* **49**, 461–470 (1997).

136. E. D. Feigelson, P. Broos, J. A. Gaffney III, G. Garmire, L. A. Hillenbrand, S. H. Pravdo, L. Townsley, Y. Tsuboi, X-ray-emitting young stars in the Orion nebula. *Astrophys. J.* **574**, 258–292 (2002).

137. H. J. Lange, T. Hahn, R. Michel, T. Schiekel, R. Rösel, U. Herpers, H. J. Hofmann, B. Dittrich-Hannen, M. Suter, W. Wölfli, P. W. Kubik, Production of residual nuclei by α-induced reactions on C, N, O, Mg, Al and Si up to 170 MeV. *Appl. Radiat. Isot.* **46**, 93–112 (1995).